1

Title: **Assessing Margin-wide Rupture Behavior along the Cascadia Megathrust using 3-D Dynamic Rupture Simulations**

Authors: Marlon D. Ramos[1], Yihe Huang[1], Thomas Ulrich[2], Duo Li[2], Alice-Agnes Gabriel[2,],
Amanda M. Thomas[3]
1. University of Michigan, Department of Earth and Environmental Sciences
2. Ludwig-Maximilians-Universität München, Department of Earth and Environmental Sciences
3. University of Oregon, Department of Earth Sciences

Social Media twitter: @QuakeMechUMich

Ramos et al

Assessing Margin-Wide Rupture Behaviors along the Cascadia Megathrust with 3-D Dynamic Rupture Simulations

Marlon D. Ramos[1], Yihe Huang[1], Thomas Ulrich[2], Duo Li[2], Alice-Agnes Gabriel[2], Amanda M. Thomas[3]

1. University of Michigan, Department of Earth and Environmental Sciences

2. Ludwig-Maximilians-Universität München, Department of Earth and Environmental Sciences

3. University of Oregon, Department of Earth Sciences

Corresponding author: Marlon D. Ramos (ramosmd@umich.edu)

Key Points

- We design the first fully dynamic 3-D earthquake simulations based on geodetic coupling models for the Cascadia megathrust.
- Segmentation in the stress drop is needed to produce subsidence amplitudes consistent with observed megathrust earthquakes.
- Dynamic rupture simulations demonstrate physics-based controls on margin-wide rupture.

Abstract

From California to British Columbia, the Pacific Northwest coast bears an omnipresent earthquake and tsunami hazard from the Cascadia subduction zone. Multiple lines of evidence suggests that magnitude eight and greater megathrust earthquakes have occurred - the most recent being 321 years ago (i.e., 1700 A.D.). Outstanding questions for the next great megathrust event include where it will initiate, what conditions are favorable for rupture to span the convergent margin, and how much slip may be expected. We develop the first 3-D fully dynamic rupture simulations that are driven by fault stress, strength and friction to address these questions. The initial dynamic stress drop distribution in our simulations is constrained by geodetic coupling models, with segment locations taken from paleoseismic analyses. We document the sensitivity of nucleation location and stress drop to the final seismic moment and coseismic subsidence amplitudes. We find that the final earthquake size strongly depends on the amount of slip deficit in the central Cascadia region, which is inferred to be creeping

Ramos et al

60   interseismically, for a given initiation location in southern or northern Cascadia. Several

61   simulations are also presented here that can closely approximate recorded coastal subsidence

62   from the 1700 A.D. event without invoking localized high-stress asperities along the down-dip

63   locked region of the megathrust. These results can be used to inform earthquake and tsunami

64   hazards for not only Cascadia, but other subduction zones that have limited seismic observations

65   but a wealth of geodetic inference.

66   **Plain Language Summary**

67   The largest earthquakes on Earth occur along faults that develop between two tectonic

68   plates that come into contact. Termed megathrust earthquakes, these catastrophic events are

69   responsible for generating both strong ground-shaking and tsunamis. The Cascadia megathrust

70   fault straddles the Pacific coastline of North America and from evidence in both the United

71   States and Japan, we know this fault last slipped in 1700 A.D. We have combined models of

72   strain buildup (geodetic coupling models) with state-of-the-art 3-D computer simulations to

73   understand the potential hazard of a future earthquake in Cascadia and show what factors might

74   lead to the fault slipping its entire length. We compare our simulations to geologic measurements

75   of permanent ground movement from 1700 A.D. Our results demonstrate that no matter where

76   the earthquake is allowed to start, coupling models showing strain accumulation to the top of the

77   fault easily leads to big earthquakes. We also look into what 1700 A.D. event may have looked

78   like and show several scenarios that fit the geologic data very closely. This work represents the

79   first set of 3-D simulations that use the laws of physics to see what may control the size of future

80   earthquakes in Cascadia.

81   **1. Introduction**

82   The Cascadia subduction zone megathrust dominates earthquake hazard in the United

83   States Pacific Northwest. It is oft-cited that the probability of a magnitude ~9 (M9) event

84   occurring in the coming decades is between 10 – 14 % (Peterson et al., 2014). The most recent

85   megathrust rupture in Cascadia occurred in 1700 A.D. and generated a transoceanic tsunami

86   (Heaton and Hartzell, 1987). Matching amplitudes of historical tsunami records from Japan

87   requires a magnitude between M8.7 - 9.2 for this earthquake (Satake et al., 1996, 2003). While

88   321 years have elapsed since this last event, the Holocene (<12 kya) earthquake record onshore

89   and offshore documents even older M > 8 megathrust events. (e.g., Atwater and Griggs, 2012;

90   Leonard et al., 2010; Kemp et al., 2018; Goldfinger et al., 2012, 2017).

Ramos et al

91 *Geological and Geophysical Inferences on the State of Megathrust Segmentation*

92   Several geological and geophysical observations suggest the Cascadia megathrust

93 exhibits along-strike segmentation. For instance, there are systematic changes in the accretionary

94 wedge backstop geometry, seismicity, and interseismic slip patterns (e.g., Stone et al., 2018;

95 Bartlow, 2020; Watt and Brothers, 2020) that may indicate coseismic rupture patterns will also

96 be variable along-strike. The strongest observational constraints that may inform our

97 understanding of future great earthquakes come from paleoseismic and geodetic observations.

98 Underwater turbidite deposits, which can be generated from submarine landslides induced by

99 strong ground-shaking during megathrust earthquakes, have been extensively used to map along-

100 strike rupture extents (Goldfinger et al., 2003; 2012; 2017; Figure 1a). Analysis of the timing and

101 spatial extents of turbidite deposits suggests that the recurrence interval (RI) between megathrust

102 earthquakes could vary along the Cascadia margin. In particular, the RI estimated for northern

103 Cascadia (> ~46°latitude) exceeds 400 years whereas it is estimated to be less than 200 years for

104 the southern portions of Cascadia (<~43°latitude; Goldfinger et al., 2017).

105   Decadal scale interseismic velocities measured at the Earth's surface by Global

106 Navigation Satellite System (GNSS) networks, tide gauge, and leveling data also find significant

107 variations in coupling (slip deficit) distribution along the margin. Regions in northern and

108 southern Cascadia have higher coupling suggesting they are accumulating strain that may be

109 released in a future great earthquake (Schmalzle et al., 2014; Li et al., 2018; Yousefi et al., 2020;

110 Figure 1b, c). However, the use of geodetic coupling inversions to place bounds on the future

111 down-dip or along-strike rupture extent is complicated by heterogeneous frictional properties

112 (Boulton et al., 2019) or the potential presence of stress shadows (Hetland and Simons, 2010;

113 Alemeida et al., 2018) and other factors (e.g., off-fault deformation). Therefore, the down-dip

114 extent of coupling and coseismic rupture may differ even though these inversion results are the

115 best available constraint on potential stress distributions for the Cascadia megathrust (Wang and

116 Trehu, 2016).

117   Another piece of evidence for segmentation comes from the behavior of episodic tremor

118 and slip (ETS) events along the megathrust. In GNSS displacement records, ETS manifests as

119 transient reversals in displacement indicative of slip on or near the megathrust at depths between

120 30 and 40 km. These slow slip episodes are often accompanied by a weak seismic signature

121 known as nonvolcanic tremor (Rodgers and Dragert, 2003). The character of ETS events varies

Ramos et al

122 significantly along the margin. The northern (i.e., > 47°) and southern (< 43°) sections host more

123 frequent slip episodes with average recurrence intervals of 10 and 14 months and have higher

124 tremor density, whereas the central section of the megathrust hosts ETS approximately every 19

125 months (Brudzinski and Allen, 2007; Wech and Creager, 2008). Studies of the ETS source

126 region find that the phenomenon occurs in regions of significantly elevated Vp/Vs ratios (e.g.,

127 Audet et al. 2009; Delph et al. 2021) and that tremor, and constituent low-frequency earthquakes,

128 are extremely sensitive to small magnitude stress changes such as those from the solid Earth

129 tides (Royer et al. 2015). Collectively, these observations suggest that pore fluid pressures are

130 nearly lithostatic in the ETS source region. The Cascadia megathrust also features a transition

131 zone at depth that separates the ETS region from the region that is conventionally considered to

132 be locked (≤20 km; Hyndman, 2013). Known as the gap, this spatial disconnect in slip behavior

133 is also found in other subduction zones (Gao and Wang, 2017); the frictional behavior and shear

134 stress accumulation levels in the gap may or may not allow for deeper rupture (Ramos and

135 Huang, 2019).

136 *Cascadia Earthquake Source Models*

137   What are ways to anticipate how a future Cascadia megathrust earthquake may behave?

138 One way to assess the hazard posed by large seismic events in Cascadia is to use kinematic

139 rupture simulations. Kinematic rupture simulations are commonplace due to the straightforward

140 relationship between fault slip and the recorded elastic displacement field once the Green's

141 functions are known, allowing these types of models to be run at lower computational cost.

142 Using the kinematic framework, potential locations of strong-ground motion sources along the

143 fault, sedimentary basin amplification or tsunami generation have been assessed (Olsen et al.,

144 2008; Delorey et al., 2014; Wirth et al., 2018; Frankel et al., 2018; Melgar et al., 2016; Roten et

145 al., 2019; Wirth et al., 2019 a, b). Most of these kinematic rupture models calibrate first-order

146 rupture parameters (slip, slip-rate, rise-time or rupture speed) from the few large megathrust

147 earthquakes observed in other subduction zones (e.g., M8.2 2003 Tokachi-Oki, M9.2 2004

148 Sumatra-Andaman, M8.8 2010 Maule, M9.1 2011 Tohoku-Oki). Kinematic simulations provide

149 important constraints on strong ground motions felt onshore, but because they must assume a slip

150 distribution before computing the elastic wavefield they cannot answer *what* controls the final

151 rupture size.

5

Ramos et al

152   To account for source physics, fully dynamic rupture simulations can be used to

153   investigate what controls the final rupture size and kinematic rupture properties like rupture

154   speed. Dynamic rupture simulations are self-consistent, physics-based numerical models that

155   describe the entire earthquake rupture process (nucleation, propagation, and arrest) that is

156   coupled a constitutive fault friction law (e.g., Madariaga and Olson, 2008). To date, 2-D dynamic

157   rupture models in Cascadia have focused on tsunami generation (e.g., Lotto et al., 2018) or how

158   frictional and stress conditions in the transition zone may influence down-dip rupture extent

159   (Ramos and Huang, 2019).

160   Here we develop 3-D dynamic rupture simulations to explore how variable strain

161   accumulation rates, frictional behavior and hypocenter location influence megathrust rupture

162   dynamics. We will use geodetic coupling results from Schmalzle et al. (2014), who utilized

163   GNSS time series information spanning several decades for their coupling inversions. These

164   coupling distributions represent two possible end-member scenarios for strain accumulation near

165   the deformation front: either there is interseismic creep at shallow megathrust depths (hereafter

166   referred to as the Gaussian coupling model; Figure 1b) or it is fully coupled (hereafter referred to

167   as the Gamma coupling model; Figure 1c). Specifically, these coupling models will be used to

168   estimate the dynamic stress drop, which is defined as the difference between the initial shear

169   stress and dynamic fault strength. Dynamic stress drop is a key parameter determining how much

170   energy is available for rupture propagation (Kanamori and Rivera, 2004). Our dynamic stress

171   drop levels are further constrained by strain accumulation times and segment locations adopted

172   from paleoseismic studies (i.e., Goldfinger et al., 2017; Figure 1a). We compare the resulting

173   coseismic uplift and subsidence patterns to available paleoseismic measurements and discuss

174   which classes of models allow margin-wide ruptures to develop. We find the final earthquake

175   size is sensitive to earthquake nucleation location (e.g., northern vs. southern Cascadia) and the

176   distribution of relative dynamic stress drop. The principal control on margin-wide rupture, when

177   using these particular end member geodetic coupling models, is the relative dynamic stress drop

178   amplitude in the central Cascadia region (~43 - 47°latitude). The results also suggest that Gamma

179   coupling models tend to produce larger earthquakes, even if shallow subducted sediment has a

180   slip-strengthening or velocity-strengthening frictional behavior. Another intriguing question is if

181   geodetic coupling models can inform our understanding about the 1700 A.D. earthquake when

182   incorporated into a dynamic rupture simulation. To that end, we also present several rupture

Ramos et al

183   simulations that provide a close fit to the 1700 A.D. event.

184
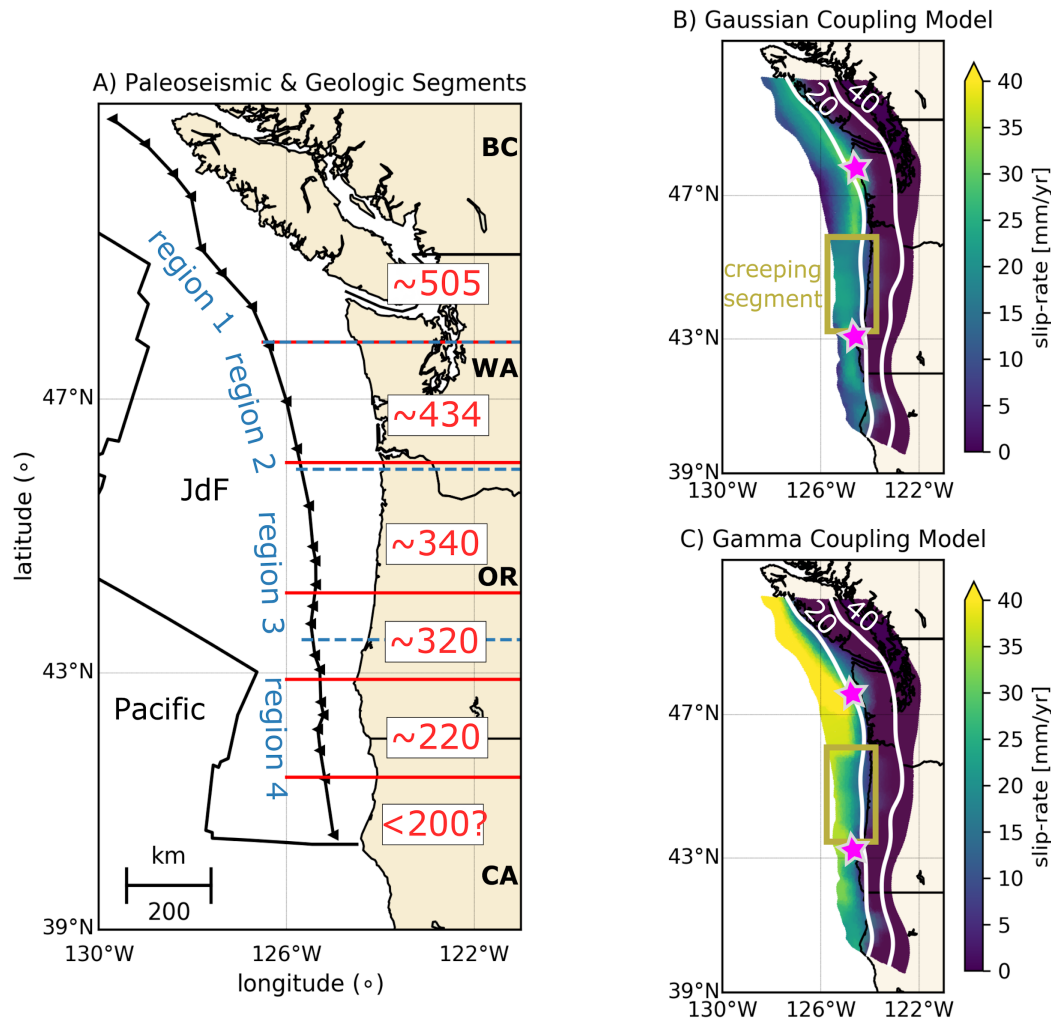
Figure 1.

Cascadia subduction zone study area. A) Megathrust segmentation (segments are separated by red lines) suggested from offshore turbidite deposits (Goldfinger et al., 2017) with corresponding estimated segment recurrence intervals in years. Primary morphotectonic regions identified by Watts and Brothers (2020) are superposed (blue dashed lines). B) Gaussian and C) Gamma coupling models from Schmalzle et al., (2014) projected onto the Slab2 megathrust geometry. The Gaussian coupling model assumes interseismic creep at shallow megathrust depths whereas the Gamma model assumes high strain accumulation. The inferred region of the creeping segment is denoted by a yellow box. Magenta stars denote rupture initiation locations in our dynamic rupture models. Thick white lines are megathrust depth contours (kilometers). JdF = Juan de Fuca plate.

193

2. Methodology

195   We solve for 3-D elastodynamic earthquake rupture using SeisSol, a powerful open-

196   source software package that implements the Arbitrary high-order DERivative-Discontinuous

Ramos et al

197 Galerkin (ADER-DG) approach to simulate wave propagation coupled to spontaneous dynamic

198 rupture (de la Puente et al., 2009; Pelties et al., 2012; Heinecke et al., 2014; Uphoff et al.,

199 2017). The capability of SeisSol to solve for complex source dynamics and incorporate realistic

200 geometric features, such as bathymetry, topography and fault zone structure (e.g., Ulrich et al.,

201 2019a, b; Wollherr et al., 2019) nicely lends itself to our purposes of investigating how

202 heterogeneous megathrust stresses influence rupture behavior.

203 We generate an unstructured 3-D tetrahedral mesh for the Cascadia subduction zone that

204 spans over 1100 km along-strike (39.0 to 51.0 degrees latitude, -127.5 to -121.0 degrees

205 longitude) and we use static refinement to increase resolution locally. The average on-fault

206 element edge size (h) is 2.5 km, and the maximum depth of the fault mesh is 50 km (Hayes et al.,

207 2018) and includes over 440,000 unstructured triangular elements. We account for the large-

208 scale variations in the free-surface geometry by meshing the ETOPO1 topography and

209 bathymetry dataset to ~1 km average element size near the coastline. In all of our simulations,

210 we use ADER-DG with fifth order accuracy (polynomial order p = 4) in time and space.

211 We ensure simulation results are sufficiently resolved by following the procedure

212 established in Wollherr et al. (2018) to estimate the process zone, the region behind the rupture

213 front where the fault strength drops from its static to dynamic level. For the 2.5-km fault mesh,

214 the median process zone width(Λ_m) is ~1.1 km. The recommended number of elements needed

215 to resolve Λ_m in a purely elastic setup with depth-dependent initial conditions is 2 - 3 (p = 4). The

216 quadrature points approach utilized in SeisSol (Pelties et al., 2014) ensures each element edge

217 length is sampled p + 2 times. Given our setup, Λ_m is sampled by ~2.7 elements which is within

218 the recommended range. The expected relative percent error in the rupture arrival time, peak

219 slip-rate, and final slip are 0.09, 8.32, and 0.71, respectively (Wollherr et al., 2018). While the

220 peak slip-rate relative error is slightly larger than the 7% recommended by Day et al., (2005) for

221 elastic rupture problems, we compare our model-predicted slip and rupture size to higher

222 resolution meshes with h = 1 km and h = 0.5 km and observe negligible changes, which gives us

223 confidence that these first order rupture features are correctly resolved. The highest resolution

224 mesh has more than 50 million elements and requires 22 hours on 40 nodes of the supercomputer

225 SuperMUC-NG at the Leibniz Supercomputing Centre, Germany.

226

227

Ramos et al

228   *2.1 Constraining dynamic rupture with geodetic coupling models*

229   In our simulations, potential shear stress distributions are informed by geodetic coupling

230   models. The Schmalzle et al., (2014) inversion for slip rate deficit was performed with respect to

231   a Cascadia megathrust geometry predating Slab2 (McCrory et al., 2012) and as such, we first

232   map the geodetic coupling models to our megathrust geometry through a bilinear interpolation

233   using the cartesian horizontal plane coordinates. But the effect of this transformation does not

234   distort the main features of the coupling models (Figure 1b, c).

235   We define the parameter T as the time needed for a certain level of slip deficit to

236   accumulate on a section of the megathrust. The product of slip rate deficit (coupling) and T is

237   slip deficit. T should not be interpreted as the RI, but rather as another way to quantify relative

238   dynamic stress drop along the megathrust. From these slip distributions, we estimate the static

239   stress drop using Poly3D, a three-dimensional, polygonal element, displacement discontinuity

240   boundary element method, which accounts for nonplanar megathrust geometry and the free-

241   surface effect due to buried slip (Thomas, 1993).

242   Initial shear stress is then estimated by adding the static stress drop to the dynamic fault

243   strength. Calculating the initial shear stress in this manner is known as the complete stress drop

244   assumption and assumes that slip deficit is accumulated linearly in the along-dip fault dimension

245   and will be entirely released during coseismic rupture (Yang et al., 2019a, b; Hok et al., 2011).

246   This shear stress distribution is first resampled to an average grid spacing of ~ 3 km and then

247   linearly interpolated onto the fault mesh. We note that we initialize stress values and friction

248   parameters with a high order sub-element resolution (e.g., Pelties et al., 2014). For all dynamic

249   rupture simulations considered, we compare the results to the 1700 A.D. subsidence

250   measurements along the coast where available (Wang et al, 2013), and to recorded subsidence

251   amplitudes from other ~M9 earthquakes (e.g., 2011 Tohoku, 1960 Chile, 1964 Alaska).

252   *2.2 Material Properties and Fault Strength*

253   Wave propagation is simulated within a heterogenous, linearly elastic medium where the

254   elastic moduli (lame parameters) vary as a function of depth. The average 1-D velocity structure

255   is taken from the Cascadia 3-D Community Velocity Model (3D-CVM) for P and S waves

256   (Figure 2a; Stephenson et al., 2017). Since the goal of this study is to calculate upper plate

257   deformation and rupture extent (along-dip and along-strike) for a given dynamic stress drop

258   distribution, we believe this is a satisfactory simplification to make. We estimate that we can

Ramos et al

259   resolve a cutoff seismic frequency up to ~0.4 Hz in the near fault region. High frequency (>1 Hz)

260   broadband ground motions can be calculated at a higher computational cost if an appropriate 3-D

261   velocity model is utilized. The current 3D-CVM was developed with respect to an older

262   Cascadia subduction zone geometry (i.e., McCrory et al., 2012) and thus, we leave direct

263   extrapolation of this 3-D velocity model to our model geometry for future work.
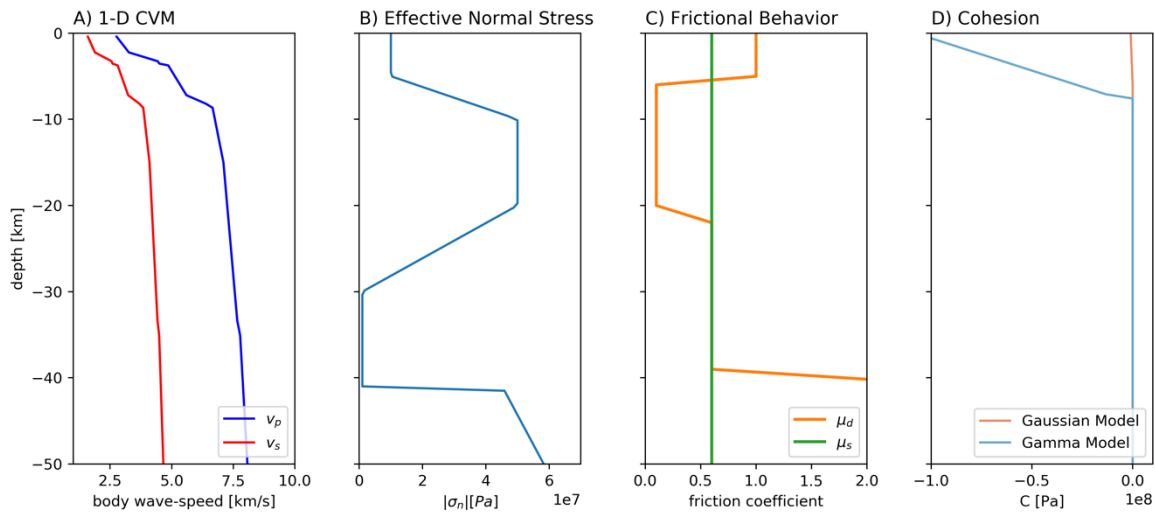
264

265   **Figure 2.** Material properties, strength, and frictional conditions for dynamic rupture simulations. A) Smoothed 1-D CVM velocity

266   model for Cascadia (Stephenson et al., 2017). B) Effective normal stress extended beyond 40 km depth from Ramos & Huang

267   (2019). C) Dynamic and static frictional coefficients with depth. D) Frictional cohesion for the Gaussian and Gamma coupling

268   models.

269   Effective normal stress accounts for pore pressure counteracting vertical lithostatic stress

270   on the fault. We use the depth-dependent effective normal stress distribution for Cascadia

271   presented in Ramos & Huang (2019) that includes low strength levels (1 MPa) in the ETS region

272   (Figure 2b). These incredibly low effective stress conditions in the ETS region are supported by

273   observations on the sensitivity of tremor and low-frequency earthquakes to small magnitude

274   stress changes (e.g., Rubinstein et al., 2007; Royer et al., 2015), stress orientations in the ETS

275   region (e.g., Newton and Thomas, 2020), and low stress drops of ETS events (e.g., Gao et al.,

276   2012). For lack of in-situ fault stress information, we assume a linear stress gradient above and

277   below the locked region (10 – 20 km depth) that are consistent with other Cascadia megathrust

278   simulations (Liu and Rice, 2009; Li and Liu, 2016). Such assumptions are simple but allow us to

279   focus on how heterogeneous shear stresses on the megathrust contribute to first order rupture

280   characteristics.

10

Ramos et al

281 *2.3 Fault friction law*

282   The physics controlling the inelastic breakdown process in our dynamic simulations is

283 given by a nonsingular linear slip-weakening friction law (Palmer and Rice, 1973). This

284 constitutive friction law allows us to idealize rupture as a propagating shear-crack. It is described

285 by the static (μ_s) and dynamic (μ_d) friction coefficients and a critical slip-weakening distance

286 (D_c).

287   We set $\mu_s = 0.6$ and $\mu_d = 0.1$ within the locked region of the megathrust (5 km ≤ depth ≤

288 20 km) [Figure 2c]. Because Ramos & Huang (2019) showed that rupture can penetrate the gap

289 or generate strong free-surface reflections if its frictional behavior is slip-weakening at depths <

290 5 km and at depths > 25 km (together with a highly negative stress drop), we set μ_d equal to or

291 above μ_s in these regions (Figure 2c). D_c is set to a constant level of 1 m or 2 m. $D_c = 2$ m is

292 selected in the dynamic rupture model in which the stress and strength conditions of Ramos &

293 Huang (2019) are extrapolated along strike, for consistency with the 2-D dynamic rupture

294 simulations. $D_c = 1$ m is used for the dynamic rupture models based on the heterogeneous

295 geodetic coupling prestress distributions. Our range of D_c values are consistent with those used

296 in slip-weakening simulations of the Tohoku-Oki earthquake, which constrained D_c using the

297 frequency range of back-projection results (Huang et al., 2014). We make minimalistic

298 assumptions for cohesion in the upper 5 km of the megathrust (Figure 2d). Due to the nearly zero

299 dynamic stress drop amplitudes near the deformation front for Gaussian coupling models, the

300 cohesion gradient can be low (Figure 2d). But in the case of the Gamma coupling models,

301 relatively higher cohesion levels (~ 5 MPa average) are locally needed at shallow fault depths to

302 prevent fault failure at the start of the simulation (Figure 2d).

303 *2.4 Rupture Initiation*

304   Fault pre-stress conditions influence the estimated critical nucleation size when using a

305 linear slip-weakening friction law. The theoretical critical nucleation radius that permits

306 spontaneous dynamic rupture to initiate in a 3-D linearly elastic and homogeneous media has

307 been derived by Day (1982) and is given by,

308
$$r_c^t = \frac{7\pi}{24} \frac{G(S+1)D_c}{\Delta\tau_d} \tag{1}$$

Ramos et al

309   where G is the shear modulus, S is the relative fault strength defined as the ratio between

310   strength excess (static fault strength minus initial shear stress) and dynamic stress drop ($\Delta\tau_d$).

311   Expression (1) provides a sufficient means to initiate and sustain dynamic rupture propagation

312   for the 3-D dynamic rupture model that is adapted from 2-D dynamic rupture simulations

313   presented in Ramos & Huang (2019). For the prestress distributions derived from the

314   heterogeneous coupling models, we determine the best numerical nucleation size through a trial-

315   and-error approach. We find that critical nucleation radii are within ~10% of the theoretically

316   predicted value calculated from equation (1). Rupture initiation is prescribed by a smooth space

317   and time dependent function, leading to an imposed rupture velocity that decreases away from

318   the hypocenter and allows a gradual transition from forced to spontaneous rupture (Harris et al.,

319   2018). Rupture nucleation locations are chosen within the areas containing the highest dynamic

320   stress drop distribution (see Figure 1b and c). Each dynamic rupture simulation is run for 420

321   seconds (7 minutes) to allow seismic waves to propagate to the edge of the model domain.
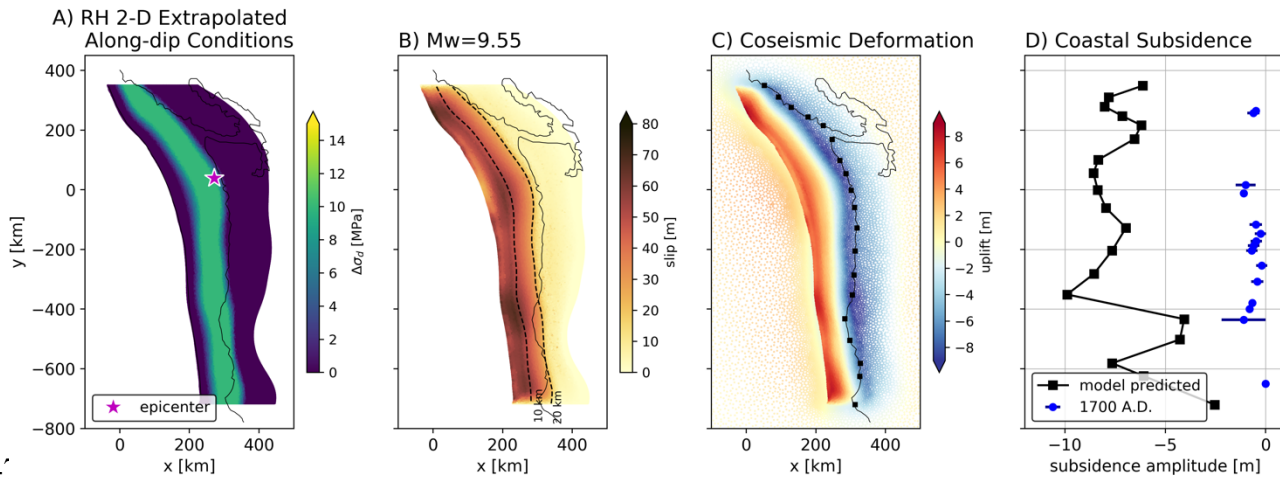
3. Results

3.1 Translating 2-D rupture simulations to 3-D

324   A 3-D dynamic rupture model that assumes a relatively homogeneous dynamic stress drop

325   profile along the locked region of the megathrust is shown in Figure 3. Previously developed 2-D

326   dynamic rupture simulations (Ramos and Huang, 2019) were relative to a specific location in

327   northern Cascadia, which is where we initiate rupture (Figure 3a). Such a laterally uniform

328   dynamic stress drop distribution is unlikely given observations of geophysical and geological

329   megathrust segmentation (e.g., Watt and Brothers, 2020). However, we develop such a simulation

330   to demonstrate 1) what a megathrust event would appear as if there was a strong gradient in shear

331   stress-rate from the locked to gap regions (20 - 30 km depth) across the margin and 2) how this

332   scenario would influence coastal subsidence amplitudes.

333   In spite of the low dynamic stress drop (<5 MPa) at depths shallower than 10 km and

334   slip-strengthening friction, coseismic slip is able to reach the deformation front with amplitudes

335   exceeding 60 m in most locations along-strike (Figure 3b). The along-strike variation of slip at

336   the deformation front exhibits two peaks north and south of the hypocenter - even though the

337   initial dynamic stress drop distribution is laterally invariant, the final coseismic slip pattern is not

338   (Figure S1). This might be attributed to changes in the along-strike megathrust dip angle. There

339   are also small amounts of slip (< 5 m) in the gap region. The coseismic hinge-line, separating

Ramos et al

340   regions of subsidence from regions of uplift, is entirely offshore (Figure 3c). Subsidence levels

341   exceeding 5 m are observed along most of the coastline (Figure 3 c, d). This exceeds subsidence

342   measurements from the 1700 A.D. event (Wang et al., 2013) by at least a factor of two because

343   the earthquake is much larger than an M9 (Figure 3d). Such subsidence amplitudes are also much

344   larger than the maximum levels observed for the 2011 M9.0 Tohoku (~1.1 m, Hashima et al.,

345   2016), 1964 M 9.4 Alaska (~ 2.4 m, Plafker et al., 1969) or the largest ever recorded event, the

346   1960 M9.5 Chile Earthquake (~2.7 m, Plafker and Savage, 1970).

347

Figure 3. Results of the dynamic rupture model in which the stress and strength conditions of Ramos & Huang (2019) are
extrapolated along-strike (RH). A) Along-strike dynamic stress drop and considered epicenter location. B) Final megathrust slip-
distribution and moment-magnitude. The black dashed lines indicate the 10 and 20 km depth whereas the solid black line denotes
the coastline. C) Coseismic uplift (red) and subsidence (blue) along the Cascadia margin. Squares signify the coastline. D) Model
predicted (black squares; same as panel C) and paleoseismic observations of estimated subsidence during the 1700 A.D. rupture
(Wang et al., 2013).

354   Interestingly, this model generates a down-dip rupture front that can reach and 'jump'

355   across the gap region, despite the negative stress drop in the gap combined with a slip-neutral

356   frictional behavior (Figure S2). Due to dynamic stress perturbations carried by seismic waves

357   ('dynamic unclamping', Oglesby and Mai, 2012; Figure S2), this down-dip rupture front is most

358   likely triggered by temporal stress changes and made possible by the incredibly low static fault

359   strength here (i.e., 0.6 MPa).

360   *3.2 Uniform Gaussian and Gamma coupling models*

361   We now explore dynamic rupture scenarios based on the Gaussian and Gamma coupling

362   models. We start with simulations that assume uniform T level (Figures 4 a and b). T is set to its

363   320 years, the time elapsed since the most recent event (Goldfinger et al, 2017). In this

Ramos et al

364   parameterization, the highest dynamic stress drop amplitude is located in the northern Cascadia

365   region for both Gaussian and Gamma distributions (Figure 4a, b), which is where spontaneous

366   rupture is initiated. The location of highest dynamic stress drop is not coincident between the

367   Gaussian and Gamma coupling models, and hence the hypocenter locations are slightly different.

368   Uniform T for both coupling models generates margin-wide rupture with coastal subsidence

369   amplitudes that again exceed 1700 A.D. (Figure 4c). The Gamma coupling model has higher

370   dynamic stress drop than the Gaussian model near the deformation front, which leads to a 1 to 2-

371   meter difference in subsidence amplitude for the northern (0 < Y < 200 km) region of the

372   megathrust (Figure 4c). These subsidence amplitudes, while lower than the 2-D extrapolated

373   model, still surpass the estimated subsidence amplitudes of the largest recorded global

374   megathrust earthquakes (i.e., 1960 Chile, 1964 Alaska). This result demonstrates that the

375   uniform T coupling model overestimates the amount of slip deficit accumulated since 1700 A.D.
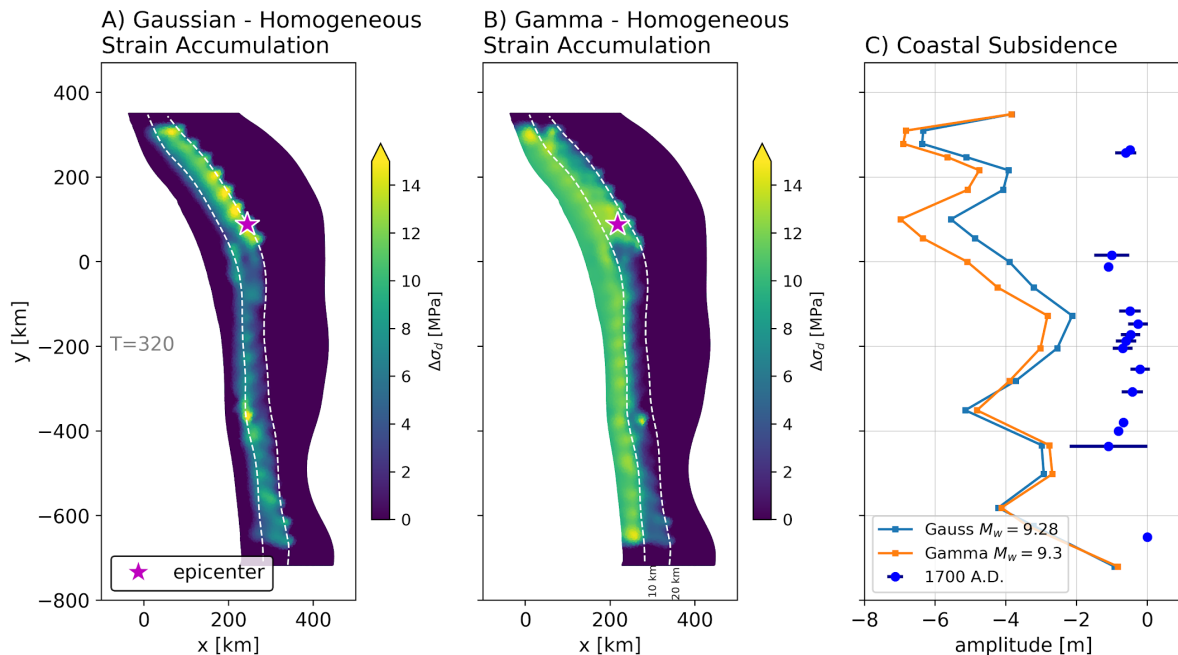
Figure 4. Comparison between Gaussian and Gamma dynamic stress drop distributions and the resultant subsidence patterns assuming the maximum strain accumulation time (T) of 320 years (i.e., time since the last great earthquake in 1700 A.D.) A) Dynamic stress drop distribution for the Gaussian coupling model. B) Dynamic stress drop distribution for the Gamma coupling model. Both ruptures are nucleated in northern Cascadia (magenta star). C) Model predicted subsidence along the coastline compared to 1700 A.D. measurements.

382   When comparing the along-dip gradient of dynamic stress drop between the simple

383   (Figure 3) and heterogeneous 3-D models (Figure 4), we note that the smoother model extends

14

Ramos et al

384 slightly deeper (Figure S2). The amplitude of coseismic subsidence is probably more strongly

385 controlled by the dynamic stress drop gradient towards the coastline (Figure S3). A point to note

386 is that the region of higher relative dynamic stress drop in the northern Cascadia region ($0 \leq Y$

387 ≤ 200 km) is also where there are limited paleoseismic measurements from 1700 A.D. Thus,

388 while geodetic coupling models are well constrained here, the few along-strike subsidence

389 measurements limit rigorous comparison to physics-based model predictions.

390 *3.3 Segmented Gaussian and Gamma coupling models*

391   We find that in order to produce coseismic uplift and subsidence amplitudes more

392 consistent with the paleoseismic Cascadia measurements and data from other megathrust

393 earthquakes (i.e., ± 2 m), we must prescribe along-strike variations of T, with T amplitudes lower

394 than 320 years for a particular segment. This is especially needed for the northern and southern

395 regions of the Cascadia megathrust, where both the Gaussian and Gamma coupling models

396 predict higher subsidence amplitudes than observed if T is set to 320 years. We refer readers to

397 the discussion section on the possible meaning of these lower T values.

398   Our partitioning of the margin is informed by paleoseismic (Goldfinger et al., 2012,

399 2017), ETS (Brudzinski and Allen, 2007), and morphotectonic studies (Watt and Brothers, 2020)

400 in Cascadia. The following dynamic rupture models are parameterized using at least three

401 segments. This choice is conservative - we found through trial-and-error that two segment

402 models cannot match first-order 1700 A.D. subsidence patterns as well as three-segment

403 models. We note that some geologic models may suggest up to five segments (e.g., Goldfinger

404 et al., 2017; Wang et al. 2013) and thus there may be multiple ways to partition T levels along-

405 strike.

406   We first study three segment rupture models that are nucleated in the northern Cascadia

407 region to see how our choice of T and segment width affect final rupture length (Figure 6a). We

408 find that placing segment limits near ~46 and 43 degrees latitude (Y ranges from 180 to -350 km;

409 Figure 5a), together with T levels between 200 – 250 years (~ 8 – 10-m slip deficit), leads to

410 margin-wide rupture. The position of these segment limits corresponds to changes in estimated

411 RI level, tremor patterns and forearc morphology (Figure 1; Goldfinger et al., 2017; Watt and

412 Brothers, 2020). The middle segment encompasses most of the creeping region offshore Oregon.

413 Holding T levels constant, we systematically move the location of the southern segment

414 boundary southward until margin-wide rupture is no longer observed. An average slip deficit of

Ramos et al

415   nearly 2 m over a width of ~80 km is needed to drive rupture through the creeping section and

416   into the southern end of Cascadia (Figure 5a). The higher coupling in the northernmost segment

417   (Y >200 km) allows for rupture to propagate north of the epicenter in all cases. In contrast, if we

418   use the Gamma coupling model, margin-wide rupture is much easier to attain even with lower

419   relative stress drop (lower T values) (Figure 5b). Lower T levels are used in the Gamma rupture

420   simulations as higher values are not required to achieve margin-wide rupture with the Gamma

421   distribution. This result demonstrates the sensitivity of margin-wide rupture to the stress level in

422   the shallow portions of the fault.   As the length of the central segment becomes shorter,

423   moment-magnitude only weakly decreases (by ~0.01) for Gamma ruptures. Gamma ruptures

424   nucleated in northern Cascadia can feature shallow, narrow slip distributions and low rupture

425   speeds ranging from ~1 to 2 km/s in the central region of the megathrust (Figure S4).

426   For dynamic ruptures initiated in southern Cascadia, we found that slightly higher T

427   levels (relative to ruptures nucleated in the north) are a necessary condition to sustain rupture

428   propagation, particularly through the central Cascadia region (Figure 5c, d). Gaussian models

429   that lead to a margin-wide rupture required an additional slip deficit of 3 m over a length of ~60

430   km in the central segment (i.e., Figure 5c, dashed line) compared to non-margin-wide rupture

431   event (i.e., Figure 5c, dot-dashed line). Similar to what was observed for ruptures initiated in

432   northern Cascadia, Gamma coupling models tend to generate margin-wide ruptures at much

433   lower slip deficit (i.e., Figure 5d). Higher relative T levels in the southernmost segment is

434   required in order for rupture to initiate and propagate outside the region of spontaneous rupture

435   initiation, given our slip-weakening friction parameters (i.e., μ_d, μ_s, Dc) and effective normal

436   stress that bound the fracture energy. The Cascadia megathrust dips more steeply below Oregon

437   and this probably influences the initial stages of ruptures that propagate from south to north more

438   than those that rupture north to south. In general, Gamma model results suggest that only a

439   narrow region of concentrated higher dynamic stress drop is sufficient for promoting margin-

440   wide rupture, even if slip-strengthening friction or higher sediment cohesion levels are

441   present. We will now discuss our assumptions about sediment friction in the shallow most

442   portions of the megathrust, and its effect on rupture size.

443

Ramos et al
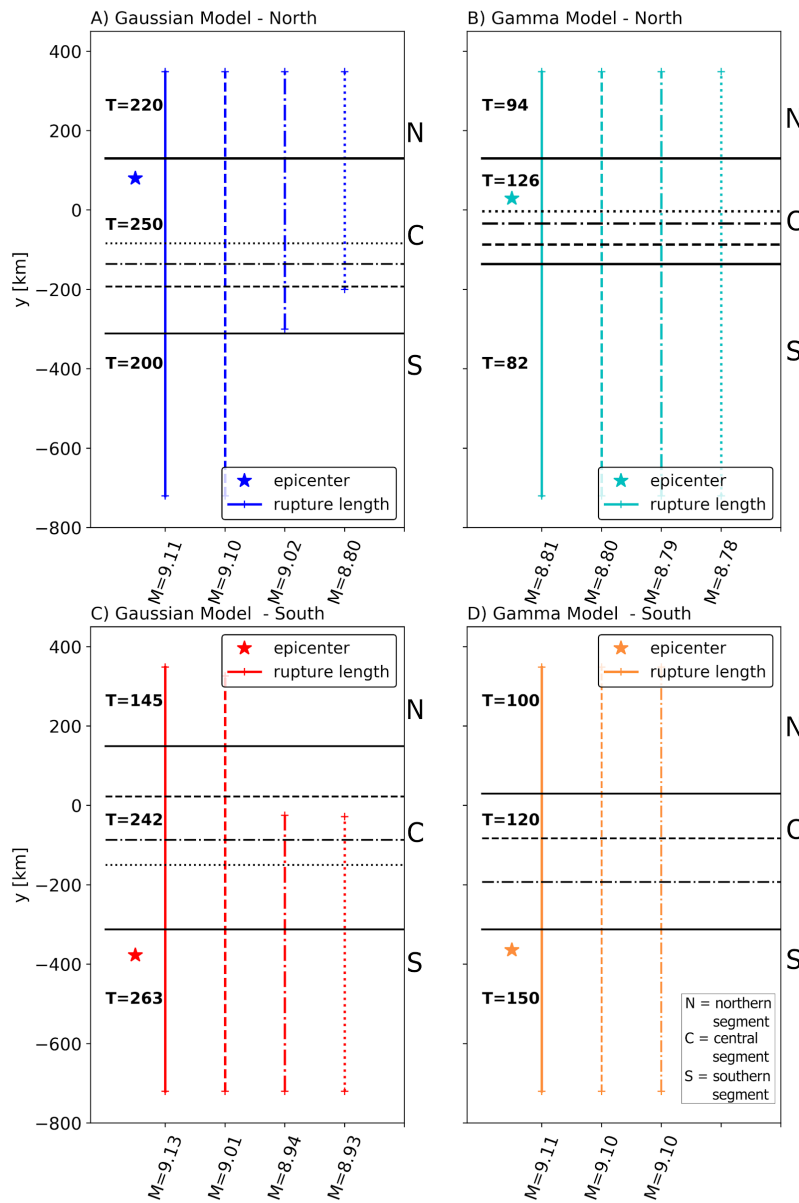
Figure 5. Gaussian and Gamma dynamic rupture simulations nucleated in northern or southern Cascadia (colored star). In each plot, the line length corresponds to the along-strike rupture extent. The line style corresponds to the variable segment location. A) Gaussian ruptures where the width of the central segment, containing the nucleation asperity, is varied until margin-wide slip no longer occurs. The T levels (relative dynamic stress drop) remains constant for each simulation. B) Same idea as A but for Gamma rupture simulations. The higher stress drop at shallower depths ($5 \leq$ km) provides enough energy for ruptures to span the entire Cascadia margin. Moment-magnitude is plotted along the x-axis on all plots. C) and D) show Gaussian and Gamma ruptures nucleated in southern Cascadia, respectively. For each subfigure, the Northern (N), central (C), or southern (S) segment regions are denoted.

Ramos et al

454   *3.4 Effect of up-dip frictional behavior*

455   In all simulations presented so far, we have assumed the influence of subducting

456   sediments will lead to slip-strengthening frictional behavior in the upper 5-km of the megathrust

457   along-strike. We now relax this assumption and let the dynamic friction level vary from slip-

458   strengthening to slip-weakening conditions (Figure 6) using the reference Gaussian model of

459   Figure 5a (solid line). In all simulations, we fix T levels and segment locations, while testing

460   varying dynamic friction coefficients in the near-margin region. Neither slip-strengthening ($\mu_d >$

461   0.6) nor slip-neutral ($\mu_d = \mu_s = 0.6$) friction leads to margin-wide rupture for this particular

462   parameterization (Figure 6a); only a slip-weakening behavior at shallow depths allows rupture to

463   spontaneously grow into a margin-wide event. The effect of dynamic friction level on slip at the

464   deformation front is shown in Figure 6b. We observe high slip amplitudes (>25 m) in northern

465   and southern Cascadia and reduced slip in central Cascadia (Figure 6b). In the margin-wide

466   rupture case (e.g., $\mu_d = 0.1$), this slip pattern is similar to other Gaussian coupling models.
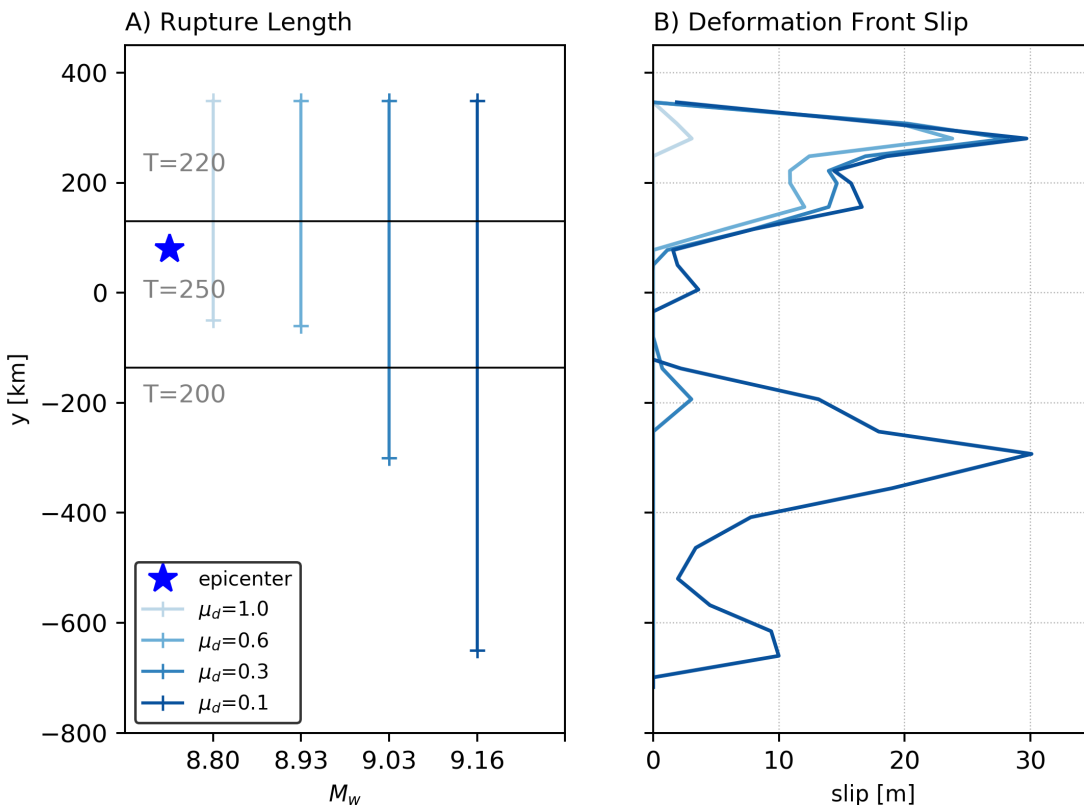
467

468   **Figure 6.** Gaussian coupling models with variable sediment frictional behavior in the upper 5 km of the megathrust. A) Along-

469   strike rupture lengths (colored lines) as function of dynamic friction coefficient. B) Slip at the deformation-front for each scenario

470   shown in A.

Ramos et al

471   *3.5 Effect of down-dip locking depth*

472   Estimating the seismogenic zone from the available geodetic data and paleoseismic

473   measurements (Hyndman, 2013; Wang and Trehu, 2016) is fraught with uncertainty because of

474   their lack of offshore resolution. In both the Gaussian and Gamma coupling models, the down-

475   dip limit of coupling (positive stress drop) is near 20 km depth (Figure 1; Schmalzle et al., 2014),

476   broadly consistent with thermal models proposed for this subduction zone (Wang et al. 1995;

477   Hyndman, 2013; Cozzens and Spinelli, 2012). To assess how locking depth influences rupture

478   width, length and subsidence amplitudes, we now relax this assumption and let locking depth

479   vary. Note that the locking depth is meant as the maximum depth where slip-weakening

480   frictional behavior exists (i.e., $\mu_d < \mu_s$). Again, we start with the three-segment Gaussian

481   simulation (Fig 5a, solid line), which does not break through the central Cascadia region (Figure

482   7a). Slip-weakening behavior with $\mu_d = 0.1$ is initially set to end at 20 km depth and we

483   systematically extend locking depth by two kilometers until 30 km (Figure 7a). A dynamic

484   rupture simulation assuming a 15-km locking depth is also shown for sake of comparison. We

485   observe that moment magnitude increases (8.8 < Mw < 9.2) due to the propagation of rupture

486   into the gap and slow-slip regions of the fault. Ruptures progressively extend further south for

487   greater locking depth, but do not become margin-wide (Figure 7a).

488   We select a 2-D profile near the hypocenter along-strike to assess how the model predicts

489   coseismic subsidence and amplitude patterns change in the margin-perpendicular direction

490   (Figure 7b). The maximum uplift and subsidence amplitudes increases by ~1 m for every 2-km

491   increase in locking depth. For deeper locking depths, the coseismic hinge-line moves closer to

492   shore, although all hinge-lines remain at least 100 km offshore for the profile selected in northern

493   Cascadia (Figure 7b).

494   *3.6 Fitting 1700 A.D. subsidence measurements*

495   Previous elastic rupture models have shown that coastal subsidence measurements from

496   1700 A.D. can be well fit with high slip-patches positioned along-strike. Wang et al., (2013) used

497   static models with four distinct asperities with T levels ranging from 450 – 550 years (18 – 22 m

498   slip deficit) to reproduce the subsidence amplitudes. In these static models, the greatest locking

499   depth was taken to taken to coincide near the 350 C isotherm as this is where silica-rich

500   lithologies would be expected to transition from velocity-weakening to velocity-strengthening

501   frictional behavior (Wang et al., 2003). 3-D kinematic simulations used a range of locking depths

19

Ramos et al

502   (~10 - 30 km) and determined that, in the presence of subevents, a locking depth near ~15 km

503   provided the strongest fit to the subsidence data (Wirth et al., 2019b).

504

505
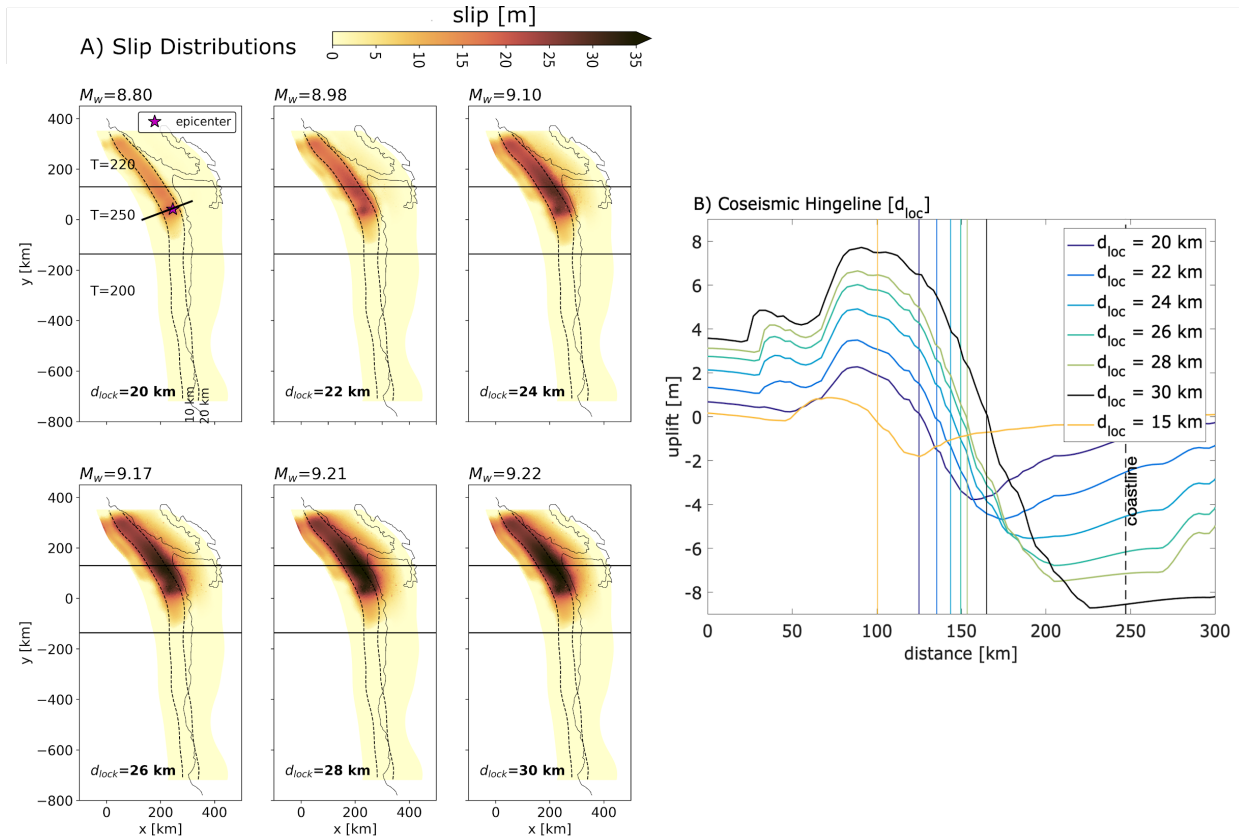
Figure 7. Effect of down-dip locking depth on coseismic slip distribution and uplift/subsidence patterns. A) Final slip distributions
for the Gaussian coupling model nucleated in northern Cascadia. The earthquake is nucleated at the red star and a profile of
uplift/subsidence at the free surface is plotted in figure B (black line through red star). In each panel, the locking depth is
systematically deepened by 2 km. B) Model-predicted coseismic subsidence and uplift for the range of locking depths studied. The
coastline is plotted for reference. Each solid line represents the coseismic hinge-line and is colored by its respective locking depth.
We also show a shallower locking depth (15 km) in yellow for comparison.

512   We present four 3-D dynamic rupture scenarios derived from Gaussian and Gamma

513   coupling distributions with a shallower locking depth at 15 km, but we also test a deeper locking

514   depth (see Discussion). The T levels and segment locations were selected through a trial-and-

515   error approach. These dynamic source models show 1700 A.D. subsidence data can be

516   reasonably fit without invoking high amplitude slip deficit or subevents (Figure 8). Ruptures

517   initiated in northern Cascadia with modest T levels ($\leq$ 250 years) can match subsidence data

518   with three segments (Figure 8a) whereas we find that four segments are required for the

20

Ramos et al

519   Gaussian rupture model initiated in southern Cascadia (Figure 8b). The Gaussian-type simulation

520   initiated in southern Cascadia has a final rupture length ~100 km shorter than the other ruptures.

521   We note that the Gaussian simulation nucleated in northern Cascadia provides the best fit to the

522   1700 A.D. subsidence data (Figure 8b, blue line).
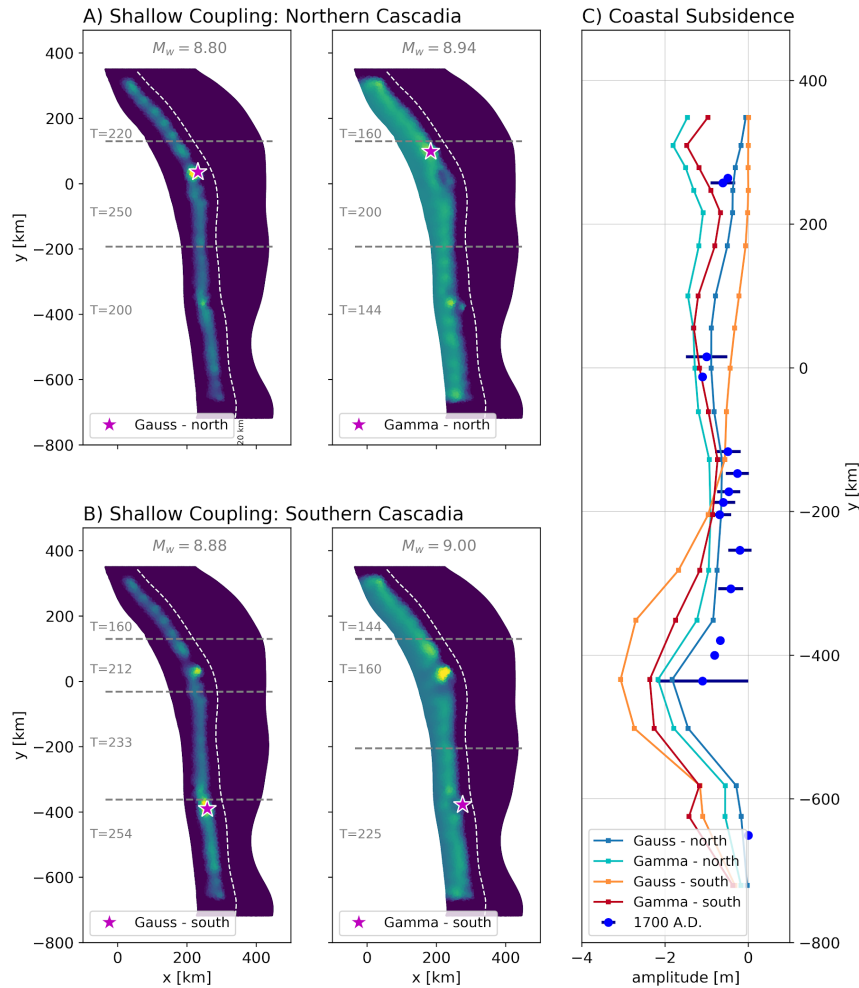
523

524   **Figure 8.** Gaussian and Gamma coupling models with shallow locking depth (15 km) that match coastal 1700 A.D. subsidence

525   measurements to first order. A) Ruptures nucleated in northern Cascadia. B) Ruptures nucleated in southern Cascadia. C)

526   Comparison of predicted coastal subsidence from simulations shown in A and B.

4. Discussion

4.1 What allows large earthquakes to develop along the Cascadia megathrust?

529   We observe margin-wide ruptures under conditions of higher relative dynamic stress drop

530   amplitudes in the inferred creeping region of the central Cascadia megathrust (i.e., higher T

Ramos et al

531 levels relative to the other segments). Alternatively, we also show that margin-wide ruptures are

532 promoted by slip weakening frictional behavior at shallow depth (Figure 6).

533   When the Gaussian or Gamma coupling models are used to generate heterogeneous shear

534 stress distributions, there are two natural locations to initiate spontaneous rupture: in northern or

535 southern Cascadia. Our results suggest that if rupture initiates in southern Cascadia, higher T

536 levels are required to sustain rupture through the central creeping region for Gaussian stress

537 distributions (Figure 5c). This is due to the combined effects from a lower slip-rate deficit

538 (inherent to both geodetic coupling models) and the generally narrower seismogenic rupture area

539 offshore Oregon caused by an increasing megathrust dip angle in this region.

540   A notable feature of our dynamic rupture simulations is that large earthquakes (M_w 8.8

541 and above) can be generated at much lower T levels than previously suggested from static

542 models (i.e., Wang et al., 2013). An explanation for this comes from dynamic effects within the

543 wedge. For instance, even though Gaussian simulations have little to no slip deficit extending to

544 the deformation front, reflections within the accretionary wedge appear to drive rupture

545 propagation along-strike. While a more realistic rheology within the wedge would certainly

546 affect wave propagation, our models suggest that wavefield inference at shallow depths could be

547 a viable mechanism to sustain rupture (Huang et al., 2014). Velocity-weakening, or in our case,

548 slip-strengthening, friction is a common assumption in dynamic rupture simulations of

549 megathrust earthquakes to represent the frictional behavior of sediments near the trench (Kozdon

550 and Dunham, 2013). One may also explicitly incorporate a subducting sediment channel

551 structure with depth-varying rigidity using slip-weakening friction (i.e., Ulrich et al., 2020). The

552 presence of clays or fluids within the megathrust fault zone can complicate the frictional

553 behavior, however (Saffer and Tobin, 2011). While Cascadia is well-known to have significant

554 sediment blanketing the trench along-strike with variable state of consolidation (Han et al.,

555 2017), there are no studies that directly sampled Cascadia megathrust fault gouge and subject

556 them to high-velocity friction experiments (Seyler et al., 2020). The assumption of slip-

557 strengthening friction in the upper 5 km in our dynamic rupture simulations is therefore modest

558 and will greatly benefit from offshore drilling data. We do not repeat the exercise of lowering the

559 dynamic friction level for ruptures in southern Cascadia, but we expect that a similar behavior

560 would occur.

Ramos et al

561   The bulk of this study explored T levels that are below 320 years and exhibit

562   segmentation along-strike. It is geologically reasonable to presume the convergence rates of the

563   Juan de Fuca and Gorda plates have been stable for ~0.78 Ma (Demets et al., 2010). When

564   megathrusts ruptures occur, they can relieve the accumulated slip deficit partially or completely

565   (Hardebeck et al., 2012). Given this assumption, our results could be interpreted to mean that the

566   slip-rate deficit is not accumulated the same everywhere along the Cascadia megathrust. This is

567   consistent with suggested RI segmentation (e.g., Goldfinger et al., 2017), some of which may be

568   expressed as along-strike changes in fault vergence patterns and outer wedge geometry (Gulick

569   et al., 1998; Watt and Brothers, 2020). There is also the possibility that the coupling models we

570   used in our study overestimated the slip-rate deficit due to inelastic off-fault deformation (e.g.,

571   Baker et al., 2013). On the other hand, if the slip-rate deficit from plate convergence is being

572   accommodated along Cascadia at a constant rate, then in order to achieve reasonable coastal

573   subsidence amplitudes (> -2 m) our models imply a partial stress drop during the 1700 A.D.

574   event. We also lack precise constraints on the absolute shear stress and fault strength levels, for

575   which we had to make reasonable assumptions in order to estimate the relative dynamic stress

576   drop. Because there are no geophysical recordings of the 1700 A.D event, a detailed slip

577   inversion will remain out of reach. However, studies have inferred potential far-field tsunami

578   patterns of this earthquake using simple kinematic rupture models and Japanese written records

579   (e.g., Satake et al., 2003; 2020). Seafloor deformation predicted from dynamic rupture models

580   may be readily incorporated into kinematic tsunami propagation simulations - differences in

581   nucleation or peak slip locations (Figure 8) may alter our understanding of historic tsunamigenic

582   earthquakes in Cascadia.

583   *4.2 Explaining 1700 A.D. subsidence patterns with Dynamic Rupture Simulations*

584   The geodetic coupling models we use show positive stress drop down to ~20 km depth

585   (Figure 1). On the other hand, 3-D kinematic simulations were able to match 1700 A.D.

586   subsidence data assuming positive stress drop does not extend deeper than a fixed coupling level

587   closer to 15 km depth (i.e., 1 cm/yr contour from Burgette et al., 2009; McCaffrey et al., 2013;

588   Wirth et al., 2019b). We show that dynamic rupture simulations which taper stress drop to 0 MPa

589   below 16 km depth can agree well with the 1700 A.D subsidence data, particularly for ruptures

590   initiated in northern Cascadia (Figure 8). While shallower locking depths generally provide a

591   stronger fit to the paleoseismic data, we were also able to construct a dynamic rupture simulation

23

Ramos et al

592 with a 20-km locking depth that fits the data just as well (Figure S5). This result suggests that if

593 T levels are sufficiently low along the fault, the subsidence patterns can probably be fit by an

594 even deeper locking depth (> 20 km depth). The influence of a deeper locking depth is to move

595 the coseismic hinge-line landwards and increase the amplitude of subsidence and uplift (i.e.,

596 Figure 7b). As discussed in Kanda and Simons (2012), either the location of peak interseismic

597 uplift-rate or greatest coseismic subsidence can provide a stronger constraint on the extent of

598 coupling as opposed to the hinge-line. Unfortunately, both the interseismic uplift (i.e., Krogstad

599 et al., 2016) and paleoseismic subsidence data (i.e., Wang et al., 2013) are limited in the along-

600 dip direction for this subduction zone. We thus caution using only paleoseismic subsidence data

601 to uniquely constrain the down-dip rupture limit in Cascadia.

602 *4.3 The Potential of Heterogeneous Down-dip Frictional Properties*

603 　　　　The next Cascadia megathrust rupture may or may not include high-frequency seismic

604 energy radiated near the down-dip limit of slip (e.g., Lay, 2015), but one way to accomplish this

605 is to superimpose high stress drop subevents (>15 MPa) at several locations along-strike (Figure

606 9). For these simulations, we assume a locking depth of 15 km. The influence of subevents,

607 compared to a coupling model with no subevents, is to increase the subsidence amplitude and

608 generate higher relative seismic frequencies.

609 　　　　To conceptually demonstrate that heterogeneous D_c can also generate relatively higher

610 seismic frequencies in the specific case of the Cascadian margin, we also design a dynamic

611 rupture simulation containing several 16 km^2 asperities near the down-dip edge of the locked

612 megathrust that have lower D_c =1 m with D_c =2m everywhere else (Figure S6). These D_c levels

613 are chosen to be consistent with already presented 3-D rupture simulations that can resolve the

614 cohesive zone widths. In this particular model, the effect of a heterogeneous D_c distribution is to

615 increase waveform amplitudes and high-frequency energy, with stations further away from the

616 hypocenter showing this more clearly (Figure S6).

617 　　　　What is unclear are properties most conducive to generating high frequency seismic

618 radiation down-dip, but dynamic rupture simulations for the 2011 Tohoku-Oki earthquake

619 showed that heterogeneous frictional properties or strength distributions (Huang et al., 2014;

620 Galvez et al, 2014) might account for these observations. We note that Cascadia is remarkably

621 different from the Japanese or Chilean subduction zones. In particular, the subducting interface

622 of the Juan de Fuca plate is relatively smooth along most of the margin compared to in the

Ramos et al

623 aforementioned regions (van Rijsingen et al., 2018) and consequently, the interface topography

624 may not provide an obvious explanation for future high seismic frequencies radiated down-dip.
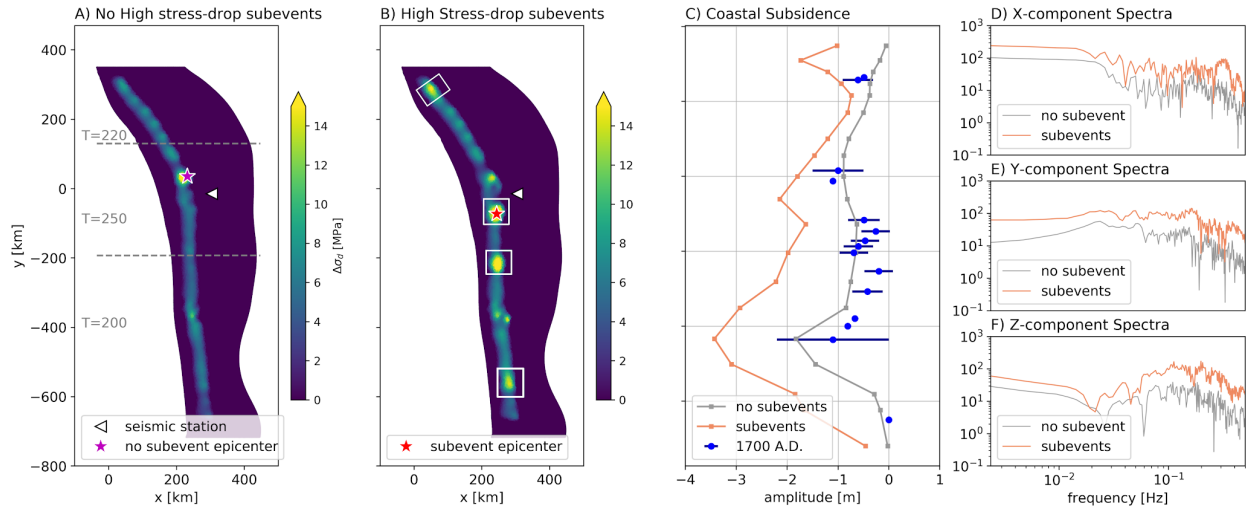
625

626 **Figure 9.** Comparison between dynamic rupture simulations with and without high dynamic stress drop subevents positioned near

627 the down-dip edge of locking (~15 km) along-strike. A) Gaussian dynamic stress drop distribution without subevents. White

628 triangle denotes synthetic seismogram receiver location. B) Gaussian dynamic stress drop distribution with superposed ~15 – 20

629 MPa subevents (white boxes). C) Coastal subsidence for both models with 1700 A.D. observations for comparison. D), F), and E)

630 show the raw spectral amplitudes of the x-, y-, and z-component velocity seismograms, respectively. The influence of the subevents

631 is to increase the high-frequency amplitudes recorded (bold colored lines).

4.4 Limitations and Future Directions

633 Our study incorporates a physically consistent source model that emphasizes the

634 importance of frictional and stress conditions necessary to generate M9-type ruptures. For lack of

635 detailed information on the velocity structure in the accretionary prism and the highly simplified

636 1-D CVM used, our 3-D dynamic rupture simulations do not capture accurate wave propagation

637 effects along the Cascadia margin. Forecasting accurate ground motions during megathrust

638 earthquakes is important, especially for subduction zones with limited or no seismic recordings

639 (Frankel et al., 2018; Wirth et al., 2018). Developing dynamic rupture simulations that account

640 for 3-D source, site, and path effects is one future direction that would, for instance, lead to more

641 physically informed hazard estimates (e.g., Wirth et al., 2020).

642 Another limitation of our study is the rheology assumed: a linearly elastic body. There is

643 potential for off-fault inelastic deformation in the wedge where there is a significant sediment

644 volume (Ma, 2012). We note further that our choice of a linear slip-weakening friction law

25

Ramos et al

645 allows us to assess first order along-strike and along-dip rupture limits, similar to Ramos &

646 Huang (2019). Modifying the friction law (and adjusting the finite element mesh resolution

647 accordingly) to account for strong rate-weakening would permit us to test a wider range of

648 rupture styles. Understanding what fault zone lithologies are present along the Cascadia

649 megathrust would also be helpful in assigning realistic dynamic friction levels during coseismic

650 rupture.

651   To improve the predictive capability of dynamic rupture simulations, offshore (e.g. near-

652 trench) geodetic measurements are needed. It would be particularly valuable if information about

653 the interseismic uplift-rate could be constrained offshore, to extend existing leveling data

654 onshore (Krogstad et al., 2016). This would reduce the ambiguity in geodetic coupling models

655 and improve our understanding of the spatial relationships between upper plate deformation and

656 intra-plate slip behavior (Bruhat and Segall, 2017; Watts and Brothers, 2020; Malatesta et al.,

657 2021). Our study stresses the importance of the spatial variation in coupling, especially in

658 the central Cascadia region where confirming the presence of lower coupling offshore Oregon is

659 critical for both kinematic and dynamic rupture simulation predictions.

660   Other geophysical measurements that have not been incorporated in this suite of dynamic

661 rupture simulations include inferences made about the seismogenic width from the arguably

662 highest resolution geophysical dataset available: the free-air gravity field. Basset et al., (2015)

663 observed that trench-parallel ridges in the free-air gravity anomaly field correlate well to the top

664 of slow-slip and tremor across the Cascadia forearc. If such trench-parallel features in the gravity

665 field are a proxy for down-dip rupture extent, then the transition from slip-weakening to slip-

666 strengthening frictional behavior may extend to depths greater than 20 km in some regions of

667 Cascadia. More work is needed to identify what geologic or geophysical features are most

668 indicative of future coseismic rupture limits, especially in subduction zones like Cascadia that

669 have not experienced megathrust events during the modern era of instrumentation.

670 **5. Conclusions**

671   Developing realistic seismic source models for the Cascadia megathrust is of paramount

672 importance to assist with seismic and tsunami risk mitigation. We present 3-D dynamic rupture

673 simulations that incorporate different hypotheses for megathrust strain accumulation based on

674 geodetic coupling models. We show that in order for margin-wide, 'M9' type ruptures to

675 develop, there must be a sufficiently high relative dynamic stress drop in the central Cascadia

Ramos et al

676 region. Moreover, a slip weakening behavior or moderate slip deficit close to the deformation-
677 front can greatly facilitate margin-wide ruptures. Along-strike variations in the slip deficit
678 pattern relative to the geodetic coupling models are required to match available paleoseismic
679 data in our dynamic rupture models. We note that strain accumulation times lower than those
680 suggested from paleoseismic studies provide a better fit to the subsidence data, which might
681 suggest coupling models are overpredicting the slip-rate deficit or there was incomplete stress
682 drop from the last megathrust rupture. A close fit to 1700 A.D. subsidence data can be achieved
683 using Gaussian or Gamma coupling distributions with locking depths of 15 or 20-km depth,
684 obviating the need to call upon localized, high amplitude slip asperities along the down-dip
685 region of the seismogenic zone.

686 This work is a step forward in using fully dynamic rupture simulations for seismic hazard
687 analysis where there have been no instrumentally recorded ruptures. Kinematic rupture
688 properties (e.g., rise-time, slip-rate and rupture speed) and static seafloor displacement from our
689 dynamic simulations can be readily incorporated into existing 3-D kinematic rupture simulations
690 or inform tsunami propagation and coastal inundation models.

691

692 **Data Availability Statement**
693 Simulations were conducted using the open-source software package SeisSol, freely available at
694 github.com/SeisSol/SeisSol. All simulation input and output files will be made accessible at the
695 University of Michigan data repository (UM Deep Blue) at
696 https://deepblue.lib.umich.edu/data/concern/data_sets/vq27zn759 pending approval.

697

27

Ramos et al

References

708 Almeida, R., Lindsey, E. O., Bradley, K., Hubbard, J., Mallick, R., & Hill, E. M. (2018). Can the
709   Updip Limit of Frictional Locking on Megathrusts be Detected Geodetically? Quantifying
710   the Effect of Stress Shadows on Near-Trench Coupling. *Geophysical Research Letters*, 1–
711   10. https://doi.org/10.1029/2018GL077785

712 Atwater, B. F., & Griggs, G. B. (2012). Deep-sea turbidites as guides to Holocene earthquake
713   history at the Cascadia Subduction Zone—Alternative views for a seismic-hazard
714   workshop. *US Geological Survey Open-File Report*, *1043*, 58.

715 Baker, A., Allmendinger, R. W., Owen, L. A., & Rech, J. A. (2013). Permanent deformation
716   caused by subduction earthquakes in northern Chile. *Nature Geoscience*, *6*(6), 492–496.
717   https://doi.org/10.1038/ngeo1789
718

719 Bartlow, N. M. (2020). A Long-Term View of Episodic Tremor and Slip in Cascadia.
720   *Geophysical Research Letters*, *47*(3),1–9. https://doi.org/10.1029/2019GL085303
721

722 Basset, D., & Watts, A. (2015). Gravity anomalies, crustal structure, and seismicity at subduction
723   zones: 2. Interrelationships between fore-arc structure and seismogenic behavior.
724   *Geochemistry Geophysics Geosystems*, *16*(1–2), 1541–1576.
725   https://doi.org/10.1002/2014GC005684.Key
726

727 Boulton, C., Niemeijer, A. R., Hollis, C. J., Townend, J., Raven, M. D., Kulhanek, D. K., &
728   Shepherd, C. L. (2019). Temperature-dependent frictional properties of heterogeneous
729   Hikurangi Subduction Zone input sediments, ODP Site 1124. *Tectonophysics*, *757*(October
730   2018), 123–139. https://doi.org/10.1016/j.tecto.2019.02.006

731 Breuer, A., Heinecke, A., & Bader, M. (2016). Petascale local time stepping for the ADER-DG
732   finite element method. In *Proceedings of the 2016 IEEE International Parallel and
733   Distributed Processing Symposium* (pp. 854–863). Chicago, IL.

Ramos et al

734 Brudzinski, M. R., & Allen, R. M. (2007). Segmentation in episodic tremor and slip all along
735 Cascadia. *Geology*, *35*(10), 907–910. https://doi.org/10.1130/G23740A.1

736 Bruhat, L., & Segall, P. (2016). Coupling on the northern Cascadia subduction zone from
737 geodetic measurements and physics-based models. *Journal of Geophysical Research: Solid*
738 *Earth*, *121*(11), 8297–8314. https://doi.org/10.1002/2016JB013267

739 Bruhat, L., & Segall, P. (2017). Deformation rates in northern Cascadia consistent with slow
740 updip propagation of deep interseismic creep. *Geophysical Journal International*
741 *211*(December), 427–449. https://doi.org/10.1093/gji/ggx317

742 Burgette, R. J., R. J. Weldon III, & D. A. Schmidt (2009). Interseismic uplift rates for western
743 Oregon and along-strike variation in locking on the Cascadia subduction zone, *Journal of*
744 *Geophysical Research: Solid Earth,* 114, no. B01408, doi: 10.1029/2008JB005679

745 Cozzens, B. D., & Spinelli, G. A. (2012). A wider seismogenic zone at Cascadia due to fluid
746 circulation in subducting oceanic crust. *Geology*, *40*(10), 899–902.
747 https://doi.org/10.1130/G33019.1

748 Day, S. M. (1982). Three-Dimensional Simulation of Spontaneous Rupture: The Effect of
749 Nonuniform Prestress. *Bulletin of the Seismological Society of America*, *72*(6), 1881–1902.

750 De La Puente, J., Ampuero, J. P., & Käser, M. (2009). Dynamic rupture modeling on
751 unstructured meshes using a discontinuous Galerkin method. *Journal of Geophysical*
752 *Research: Solid Earth*, *114*(10), 1–17. https://doi.org/10.1029/2008JB006271

753 Delorey, A. A., Frankel, A. D., Liu, P., & Stephenson, W. J. (2014). Modeling the Effects of
754 Source and Path Heterogeneity on Ground Motions of Great Earthquakes on the Cascadia
755 Subduction Zone Using 3D Simulations. *Bulletin of the Seismological Society of America*,
756 *104*(3), 1430–1446. https://doi.org/10.1785/0120130181

757 Delph, J. R., Thomas, A. M., & Levander, A. (2021). Subcretionary tectonics: Linking
758 variability in the expression of subduction along the Cascadia forearc. *Earth and Planetary*
759 *Science Letters*, *556*, 116724. https://doi.org/10.1016/j.epsl.2020.116724

Ramos et al

760 DeMets, C., Gordon, R. G., & Argus, D. F. (2010). Geologically current plate motions.

761 *Geophysical Journal International*, 181(1), 1–80. https://doi. org/10.1111/j.1365-

762 246X.2009.04491

763 Frankel, A., Wirth, E., Marafi, N., Vidale, J., & Stephenson, W. (2018). Broadband Synthetic

764 Seismograms for Magnitude 9 Earthquakes on the Cascadia Megathrust Based on 3D

765 Simulations and Stochastic Synthetics, Part 1: Methodology and Overall Results. *Bulletin of*

766 *the Seismological Society of America*, *108*(5), 2347–2369.

767 https://doi.org/10.1785/0120180034

768 Galvez, P., Ampuero, J. P., Dalguer, L. A., Somala, S. N., & Nissen-Meyer, T. (2014). Dynamic

769 earthquake rupture modelled with an unstructured 3-D spectral element method applied to

770 the 2011 M9 Tohoku earthquake. *Geophysical Journal International*, *198*(2), 1222–1240.

771 https://doi.org/10.1093/gji/ggu203

772 Galvez, P., Dalguer, L. A., Ampuero, J. P., & Giardini, D. (2016). Rupture reactivation during

773 the 2011 mw9.0 tohoku earthquake: Dynamic rupture and ground-motion simulations.

774 *Bulletin of the Seismological Society of America*, *106*(3), 819–831.

775 https://doi.org/10.1785/0120150153

776 Goldfinger, C., Nelson, C. H., & Johnson, J. E. (2003). Holocene Earthquake records from the

777 Cascdia Subduction Zone and Northern San Andreas fault based on precise dating of

778 offshore turbidites. *Annual Review of Earth and Planetary Sciences*, *31*(1), 555–577.

779 https://doi.org/10.1146/annurev.earth.31.100901.141246

780 Goldfinger, C., Nelson, C.H., Morey, A., Johnson, J.E., Gutierrez-Pastor, J., Eriksson, A.T.,

781 Karabanov, E., Patton, J., Gracia, E., Enkin, R., Dallimore, A., Dunhill, G., Vallier, T.,

782 2012a. Turbidite Event History: Methods and Implications for Holocene Paleoseismicity of

783 the Cascadia Subduction Zone. *USGS Professional Paper* 1661-F (184 pp).

784 Goldfinger, C., Galer, S., Beeson, J., Hamilton, T., Black, B., Romsos, C., ... Morey, A. (2017).

785 The importance of site selection, sediment supply, and hydrodynamics: A case study of

Ramos et al

786   submarine paleoseismology on the northern Cascadia margin, Washington USA. *Marine*

787   *Geology*, *384*, 4,17,25-16,17,46. https://doi.org/10.1016/j.margeo.2016.06.008

788   Gulick, S. P. S., Meltzer, A. M. & Clarke, S. H. (1998) Seismic structure of the southern

789   Cascadia subduction zone and accretionary prism north of the Mendocino triple junction.

790   J*ournal of Geophysical Research: Solid Earth*,t 103, 27207–27222.

791

792   Harris, R. A., Aagaard, B., Barall, M., Ma, S., Roten, D., Olsen, K., … Dalguer, L. (2018). A

793   suite of exercises for verifying dynamic earthquake rupture codes. *Seismological Research*

794   *Letters*, *89*(3), 1146–1162. https://doi.org/10.1785/0220170222

795   Hashima, A., Becker, T.W., Freed, A.M. et al. Coseismic deformation due to the 2011 Tohoku-

796   oki earthquake: influence of 3-D elastic structure around Japan. *Earth Planets Space,* 68,

797   159 (2016). https://doi.org/10.1186/s40623-016-0535-9

798   Hayes, G. P., Moore, G. L., Portner, D. E., Hearne, M., Flamme, H., Furtney, M., & Smoczyk,

799   G. M. (2018). Slab2 - A Comprehensive Subduction Zone Geometry Model. *Science*,

800   (August), 1–10.

801   Heaton, Thomas H., Hartzell, S. H. (1987). Earthquake Hazards on the Cascadia Subduction

802   Zone. *Science*, *236*(4798), 162–168. https://doi.org/DOI: 10.1126/science.236.4798.162

803   Heinecke, A. et al. (2014). Petascale high order dynamic rupture earthquake simulations on

804   heterogeneous supercomputers. In SC14: *International Conference for High Performance*

805   *Computing, Networking, Storage and Analysis* 3–14 (IEEE).

806   https://doi.org/10.1109/SC.2014.6.

807

808   Hetland, E. A., & Simons, M. (2010). Post-seismic and interseismic fault creep II: Transient

809   creep and interseismic stress shadows on megathrusts. *Geophysical Journal International*,

810   *181*(1), 99–112. https://doi.org/10.1111/j.1365-246X.2009.04482.x

Ramos et al

811   Hok, S., Fukuyama, E., & Hashimoto, C. (2011). Dynamic rupture scenarios of anticipated
812   Nankai-Tonankai earthquakes, southwest Japan. *Journal of Geophysical Research: Solid*
813   *Earth*, *116*(12), 1–22. https://doi.org/10.1029/2011JB008492

814   Huang, Y., Meng, L., & Ampuero, J. P. (2012). A dynamic model of the frequency-dependent
815   rupture process of the 2011 Tohoku-Oki earthquake. *Earth, Planets and Space*, *64*(12),
816   1061–1066. https://doi.org/10.5047/eps.2012.05.011

817   Huang, Y., Ampuero, J. P., & Kanamori, H. (2014). Slip-Weakening Models of the 2011
818   Tohoku-Oki Earthquake and Constraints on Stress Drop and Fracture Energy. *Pure and*
819   *Applied Geophysics*, *171*(10), 2555–2568. https://doi.org/10.1007/s00024-013-0718-2

820   Hyndman, R. D. (2013). Downdip landward limit of Cascadia great earthquake rupture. *Journal*
821   *of Geophysical Research: Solid Earth*, *118*(10), 5530–5549.
822   https://doi.org/10.1002/jgrb.50390

823   Kemp, A. C., Cahill, N., Engelhart, S. E., Hawkes, A. D., & Wang, K. (2018). Revising
824   estimates of spatially variable subsidence during the A.D. 1700 cascadia earthquake using a
825   bayesian foraminiferal transfer function. *Bulletin of the Seismological Society of America*,
826   *108*(2), 654–673. https://doi.org/10.1785/0120170269

827   Kanamori, H., & Rivera, L. (2004). Static and dynamic scaling relations for earthquakes and
828   their implications for rupture speed and stress drop. *Bulletin of the Seismological Society of*
829   *America*, *94*(1), 314–319. https://doi.org/10.1785/0120030159

830   Kaneko, Y. & Lapusta, N., (2010). Supershear transition due to a free surface in 3-D simulations
831   ofspontaneous dynamic rupture on vertical strike-slip faults, *Tectonophysics*, 493, 272–284.

832   Krogstad, R. D., Schmidt, D. A., Weldon, R. J., & Burgette, R. J. (2016). Constraints on
833   accumulated strain near the ETS zone along Cascadia. *Earth and Planetary Science Letters*,
834   *439*, 109–116. https://doi.org/10.1016/j.epsl.2016.01.033

Ramos et al

835   Lay, T. (2015). The surge of great earthquakes from 2004 to 2014. *Earth and Planetary Science*
836   *Letters*, *409*, 133–146. https://doi.org/10.1016/j.epsl.2014.10.047

837   Lay, T., Kanamori, H., Ammon, C. J., Koper, K. D., Hutko, A. R., Ye, L., … Rushing, T. M.
838   (2012). Depth-varying rupture properties of subduction zone megathrust faults. *Journal of*
839   *Geophysical Research: Solid Earth*. https://doi.org/10.1029/2011JB009133

840   Leonard, L. J., Currie, C. A., Mazzotti, S., & Hyndman, R. D. (2010). Rupture area and
841   displacement of past Cascadia great earthquakes from coastal coseismic subsidence.
842   *Bulletin of the Geological Society of America*, *122*(11–12), 2079–2096.
843   https://doi.org/10.1130/B30108.1
844

845   Li, S., Wang, K., Wang, Y., Jiang, Y., & Dosso, S. E. (2018). Geodetically Inferred Locking
846   State of the Cascadia Megathrust Based on a Viscoelastic Earth Model. *Journal of*
847   *Geophysical Research: Solid Earth*, *123*(9), 8056–8072.
848   https://doi.org/10.1029/2018JB015620

849   Li, D., and Y. Liu (2016), Spatiotemporal evolution of slow slip events in a nonplanar fault
850   model for northern Cascadia subduction zone, J. Geophys. Res., 121(9), 6828-6845, doi:
851   10.1002/2016jb012857.

852   Lotto, G. C., Jeppson, T. N., & Dunham, E. M. (2018). Fully-coupled simulations of megathrust
853   earthquakes and tsunamis in the Japan Trench, Nankai Trough, and Cascadia Subduction
854   Zone. *Pure and Applied Geophysics*, https://doi.org/10.1007/s00024-018-1990-y Pure.
855   https://doi.org/10.1007/s00024-018-1990-y

856   Madariaga, R. & Olsen, K.B. (2002) Earthquake dynamics. In: *Int. Handbook of Earthquake and*
857   *Engineering Seismology*, vol. 81A, pp 175 - 194

858   Malatesta, L. C., Bruhat, L., Finnegan, N. J., & Olive, J. L. (2021). Colocation of the downdip
859   end of seismic coupling and the continental shelf break. *Journal of Geophysical Research:*
860   *Soild Earth*, *X*, 1–38. https://doi.org/10.2307/2609006

Ramos et al

861

862 McCrory, P. A., Blair, J. L., Waldhauser, F., & Oppenheimer, D. H. (2012). Juan de Fuca slab
863   geometry and its relation to Wadati-Benioff zone seismicity. *Journal of Geophysical*
864   *Research: Solid Earth*, *117*(9), 1–24. https://doi.org/10.1029/2012JB009407

865 Melgar, D.; LeVesque, R.-J.; Dreger, D. S.; and Allen, R. (2016). Kinematic rupture scenarios
866   and synthetic displacement data: An example application to the Cascadia subduction zone.
867   *Journal of Geophysical Research Soild Earth*, *121*, 6658–6674.
868   https://doi.org/10.1002/jgrb.50358.

869 Meng, L., A. Inbal, & J. P. Ampuero (2011). A window into the complexity of the dynamic
870   rupture of the 2011 Mw 9 Tohoku-Oki earthquake, *Geophys. Res. Lett*. 38, L00G07, doi:
871   10.1029/2011GL048118.

872 Newton, T. J., & Thomas, A. M. (2020). Stress Orientations in the Nankai Trough Constrained
873   Using Seismic and Aseismic Slip. *Journal of Geophysical Research: Solid Earth*, *125*(7), 1–
874   16. https://doi.org/10.1029/2020JB019841

875 Oglesby, D. D., & Mai, P. M. (2012). Fault geometry, rupture dynamics and ground motion from
876   potential earthquakes on the North Anatolian Fault under the Sea of Marmara. *Geophysical*
877   *Journal International*, *188*(3), 1071–1087. https://doi.org/10.1111/j.1365-
878   246X.2011.05289.x

879 Olsen, K. B., Stephenson, W. J., & Geisselmeyer, A. (2008). 3D crustal structure and long-
880   period ground motions from a M9.0 megathrust earthquake in the Pacific Northwest region.
881   *Journal of Seismology*, *12*, 145–159. https://doi.org/10.1007/s10950-007-9082-y

882 Palmer, A. C., and J. R. Rice (1973), The growth of slip surfaces in the progressive failure of over-
883   consolidated clay, *Proc. R. Soc. London,* Ser. A, 332, 527–548.

884 Pelties, C., De La Puente, J., Ampuero, J. P., Brietzke, G. B., & Käser, M. (2012). Three-
885   dimensional dynamic rupture simulation with a high-order discontinuous Galerkin method on

Ramos et al

886   unstructured tetrahedral meshes. *Journal of Geophysical Research: Solid Earth*, *117*(2), 1–15.
887   https://doi.org/10.1029/2011JB008857

888   Pelties, C., Gabriel, A.-A., and Ampuero, J.-P.(2014). Verification of an ADER-DG method for
889   complex dynamic rupture problems, Geosci. Model Dev., 7, 847–866,
890   https://doi.org/10.5194/gmd-7-847-2014, 2014.

891   Petersen, M. D., M. P. Moschetti, P. Powers, C. S. Mueller, K. M. Haller, A. D. Frankel, Y. Zeng,
892   S. Rezaeian, S. C. Harmsen, O. L. Boyd, et al. (2014). Documentation for the 2014 national
893   seismic hazard maps, *U.S. Geol. Surv. Open-File Report*, 2014-1091, 255 pp.
894

895   Phillips, B. A., Kerr, A. C., Mullen, E. K., & Weis, D. (2017). Oceanic mafic magmatism in the
896   Siletz terrane, NW North America: Fragments of an Eocene oceanic plateau? *Lithos*, 291–
897   303.

898   Plafker, George, Savage, J. C. (1970). Mechanism of the Chilean Earthquakes of May 21 and
899   22, 1960. *Geological Society of America Bulletin*, *81*, 1001–1030.

900   Plafker, G. (1972). Alaskan earthquake of 1964 and Chilean earthquake of 1960: Implications
901   for arc tectonics. *Journal of Geophysical Research*, *77*(5), 901.
902   https://doi.org/10.1029/JB077i005p00901

903   Priest, G. R., Witter, R. C., Zhang, Y. J., Goldfinger, C., Wang, K., & Allan, J. C. (2017). New
904   constraints on coseismic slip during southern Cascadia subduction zone earthquakes over
905   the past 4600 years implied by tsunami deposits and marine turbidites. *Natural Hazards*,
906   *88*(1), 285–313. https://doi.org/10.1007/s11069-017-2864-9

907   Ramos, M. D., & Huang, Y. (2019). How the transition region along the Cascadia megathrust
908   influences coseismic behavior: Insights from 2-D dynamic rupture simulations. *Geophysical*
909   *Research Letters*, *46*, 1–11. https://doi.org/10.1029/2018gl080812

910   Roten, D., Olsen, K. B., & Takedatsu, R. (2019). Numerical Simulation of M9 Megathrust
911   Earthquakes in the Cascadia Subduction Zone. *Pure and Applied Geophysics*.
912   https://doi.org/10.1007/s00024-018-2085-5

Ramos et al

913   Royer, A. A., Thomas, A. M., & Bostock, M. G. (2015). Tidal modulation and triggering of low-
914   frequency earthquakes in northern Cascadia. *Journal of Geophysical Research: Solid*
915   *Earth*, *120*(1), 384–405. https://doi.org/10.1002/2014JB011430

916   Rubinstein, J. L., Vidale, J. E., Gomberg, J., Bodin, P., Creager, K. C., & Malone, S. D. (2007).
917   Non-volcanic tremor driven by large transient shear stresses. *Nature*, *448*(7153), 579–582.
918   https://doi.org/10.1038/nature06017

919   Saffer, D. M., & Tobin, H. J. (2011). Hydrogeology and Mechanics of Subduction Zone
920   Forearcs: Fluid Flow and Pore Pressure. *Annual Review of Earth and Planetary Sciences*,
921   *39*, 157–186. https://doi.org/10.1146/annurev-earth-040610-133408

922   Sallarès, V., & Ranero, C. R. (2019). Upper-plate rigidity determines depth-varying rupture
923   behaviour of megathrust earthquakes. *Nature*, *576*(7785), 96–101.
924   https://doi.org/10.1038/s41586-019-1784-0

925   Satake, K., Shimazaki, K., Tsuji, Y., & Ueda, K. (1996). Time and size of a giant earthquake in
926   Cascadia inferred from Japanese tsunami records of January 1700. *Nature*.
927   https://doi.org/10.1038/379246a0

928   Satake, K., Wang, K., Atwater, B.F., 2003. Fault slip and seismic moment of the 1700 Cascadia
929   earthquake inferred from Japanese tsunami descriptions. *Journal of Geophysical Research:*
930   *Solid Earth*. 108, B11 2535. https://doi.org/10.1029/2003JB002521.

931   Satake, K., Heidarzadeh, M., Quiroz, M., & Cienfuegos, R. (2020). History and features of trans-
932   oceanic tsunamis and implications for paleo-tsunami studies. *Earth-Science Reviews*,
933   *202*(January), 103112. https://doi.org/10.1016/j.earscirev.2020.103112

934   Schmalzle, G. M., McCaffrey, R., & Creager, K. C. (2014). Central Cascadia subduction zone
935   creep. *Geochemistry, Geophysics, Geosystems*, *15*(4), 1515–1532.
936   https://doi.org/10.1002/2013GC005172

Ramos et al

937 Seyler, C., Kirkpatrick, J. D., Hirose, T., & Savage, H. M. (2020). Rupture to the trench?

938 Frictional properties of incoming sediments at the Cascadia subduction zone. *Earth and*

939 *Planetary Science Letters*, *546*, 116413. https://doi.org/10.1016/j.epsl.2020.116413

940 Stephenson, W. J., Reitman, N. G., & Angster, S. J. (2017). P- and S-wave velocity models

941 incorporating the Cascadia subduction zone for 3D earthquake ground motion

942 simulations—Update for Open-File Report 2007–1348. *Open-File Report*, (December), 28.

943 https://doi.org/10.3133/ofr20171152

944 Thomas, A. L. (1993), Poly3D: A Three-Dimensional, Polygonal Element, Displacement

945 Discontinuity Boundary Element Computer Program with Applications to Fractures, Faults,

946 and Cavities in the Earth's Crust, Stanford Univ., Stanford, Calif.

947 Ulrich, T., Gabriel, A. A., Ampuero, J. P., & Xu, W. (2019). Dynamic viability of the 2016 Mw

948 7.8 Kaikōura earthquake cascade on weak crustal faults. *Nature Communications*, *10*(1).

949 https://doi.org/10.1038/s41467-019-09125-w

950 Ulrich, T., Gabriel, A. A, & Madden, E. H. (2020). Stress, rigidity and sediment strength control

951 megathrust earthquake and tsunami dynamics. under revision at Nat. Geosc., preprint

952 available at EarthArxiv https://doi.org/10.31223/osf.io/s9263/*s*

953

954 Uphoff, C., Rettenberger, S., Bader, M., Madden, E. H., Ulrich, T., Wollherr, S., & Gabriel, A.-

955 A. (2017). Extreme scale multi-physics simulations of the tsunamigenic 2004 Sumatra

956 megathrust earthquake. In *Proceedings of the International Conference for High*

957 *Performance Computing, Networking, Storage and Analysis*, ACM (pp. 21).

958 van Rijsingen, E., Lallemand, S., Peyret, M., Arcay, D., Heuret, A., Funiciello, F., & Corbi, F.

959 (2018). How Subduction Interface Roughness Influences the Occurrence of Large Interplate

960 Earthquakes. *Geochemistry, Geophysics, Geosystems*, *19*(8), 2342–2370.

961 https://doi.org/10.1029/2018GC007618

37

Ramos et al

962   Wang, K., Wells, R., Mazzotti, S., Hyndman, R. D., & Sagiya, T. (2003). A revised dislocation
963   model of interseismic deformation of the Cascadia subduction zone. *Journal of*
964   *Geophysical Research: Solid Earth*. https://doi.org/10.1029/2001JB001227

965   Wang, P. L., Engelhart, S. E., Wang, K., Hawkes, A. D., Horton, B. P., Nelson, A. R., & Witter,
966   R. C. (2013). Heterogeneous rupture in the great Cascadia earthquake of 1700 inferred
967   from coastal subsidence estimates. *Journal of Geophysical Research: Solid Earth*, *118*(5),
968   2460–2473. https://doi.org/10.1002/jgrb.50101

969   Wang, K., Hu, Y., & He, J. (2012). Deformation cycles of subduction earthquakes in a
970   viscoelastic Earth. *Nature*, *484*(7394), 327–332. https://doi.org/10.1038/nature11032

971   Wang, K., & Tréhu, A. M. (2016). Invited review paper: Some outstanding issues in the study of
972   great megathrust earthquakes—The Cascadia example. *Journal of Geodynamics*, *98*, 1–18.
973   https://doi.org/10.1016/j.jog.2016.03.010

974   Watt, J., & Brothers, D. S. (2020). Systematic Characterization of Morpho-Tectonic Variability
975   Along the Cascadia Convergent Margin: Implications for Outer Wedge Dynamics and
976   Shallow Megathrust Behavior. *Geosphere*, *17*(X), 1–23.
977   https://doi.org/10.1130/abs/2019cd-329471

978   Wech, A. G., & Creager, K. C. (2011). A continuum of stress, strength and slip in the Cascadia
979   subduction zone. *Nature Geoscience*, *4*(9), 624–628. https://doi.org/10.1038/ngeo1215

980   Wirth, E., Frankel, A., Marafi, N., Vidale, J., & Stephenson, W. (2018). Broadband Synthetic
981   Seismograms for Magnitude 9 Earthquakes on the Cascadia Megathrust Based on 3D
982   Simulations and Stochastic Synthetics, Part 2: Rupture Parameters and Variability. *Bulletin*
983   *of the Seismological Society of America*, *108*(5), 2370–2388.
984   https://doi.org/10.1785/0120180034

985   Wirth, E. A., Vidale, J. E., Frankel, A. D., Pratt, T. L., Marafi, N. A., Thompson, M., &
986   Stephenson, W. J. (2019). Source-Dependent Amplification of Earthquake Ground Motions

Ramos et al

987   in Deep Sedimentary Basins. *Geophysical Research Letters*, *46*(12), 6443–6450.

988   https://doi.org/10.1029/2019GL082474

989   Wirth, E. A., & Frankel, A. D. (2019). Impact of Down-Dip Rupture Limit and High-Stress Drop

990   Subevents on Coseismic Land-Level Change during Cascadia Megathrust Earthquakes.

991   *Bulletin of the Seismological Society of America*, *XX*(Xx).

992   https://doi.org/10.1785/0120190043

993   Wirth, E. A., Grant, A., Marafi, N. A., & Frankel, A. D. (2020). Ensemble ShakeMaps for

994   Magnitude 9 Earthquakes on the Cascadia Subduction Zone. *Seismological Research*

995   *Letters*, *XX*, 1–13. https://doi.org/10.1785/0220200240.Introduction

996   Witter, R. C., Zhang, Y., Wang, K., Goldfinger, C., Priest, G. R., & Allan, J. C. (2012).

997   Coseismic slip on the southern Cascadia megathrust implied by tsunami deposits in an

998   Oregon lake and earthquake-triggered marine turbidites. *Journal of Geophysical Research:*

999   *Solid Earth*, *117*(B10), 1–18. https://doi.org/10.1029/2012jb009404

1000 Wollherr, S., Gabriel, A.-A., & Uphoff, C. (2018). Off-fault plasticity in three-dimensional

1001   dynamic rupture simulations using a modal Discontinuous Galerkin method on unstructured

1002   meshes: implementation, verification and application. *Geophysical Journal International*,

1003   *214*(3), 1556–1584. https://doi.org/10.1093/gji/ggy213

1004 Wollherr, S., Gabriel, A. A., & Mai, P. M. (2019). Landers 1992 "Reloaded": Integrative

1005   Dynamic Earthquake Rupture Modeling. *Journal of Geophysical Research: Solid Earth*.

1006   https://doi.org/10.1029/2018JB016355

1007 Yang, H., Yao, S., He, B., Newman, A., & Weng, H. (2019). Deriving rupture scenarios from

1008   interseismic locking distributions along the subduction megathrust. *Journal of Geophysical*

1009   *Research: Solid Earth*, 2019JB017541. https://doi.org/10.1029/2019JB017541

1010 Yang, H., Yao, S., He, B., & Newman, A. V. (2019). Earthquake rupture dependence on

1011   hypocentral location along the Nicoya Peninsula subduction megathrust. *Earth and*

1012   *Planetary Science Letters*, *520*, 10–17. https://doi.org/10.1016/j.epsl.2019.05.030

Ramos et al

1013   Yao, S., & Yang, H. (2020). Rupture Dynamics of the 2012 Nicoya Mw 7.6 Earthquake:

1014   Evidence for Low Strength on the Megathrust. *Geophysical Research Letters*, *47*(13), 1–11.

1015   https://doi.org/10.1029/2020GL087508

1016   Yousefi, M., Milne, G., Li, S., Wang, K., & Bartholet, A. (2020). Constraining Interseismic

1017   Deformation of the Cascadia Subduction Zone: New Insights From Estimates of Vertical

1018   Land Motion Over Different Timescales. *Journal of Geophysical Research: Solid Earth*,

1019   *125*(3), 1–18. https://doi.org/10.1029/2019JB018248

Ramos et al